AD_____

Award Number: DAMD17-99-1-9294

TITLE: Automated Spot Mammography for Improved Imaging of Dense Breasts

PRINCIPAL INVESTIGATOR: Mitchell M. Goodsitt, Ph.D.

CONTRACTING ORGANIZATION: University of Michigan
Ann Arbor, Michigan 48109-1274

REPORT DATE: October 2000

TYPE OF REPORT: Annual

PREPARED FOR: U.S. Army Medical Research and Materiel Command
Fort Detrick, Maryland 21702-5012

DISTRIBUTION STATEMENT: Approved for Public Release;
Distribution Unlimited

The views, opinions and/or findings contained in this report are those of the author(s) and should not be construed as an official Department of the Army position, policy or decision unless so designated by other documentation.

REPORT DOCUMENTATION PAGE

Form Approved
OMB No. 074-0188

1. AGENCY USE ONLY (Leave blank)	2. REPORT DATE	3. REPORT TYPE AND DATES COVERED
	October 2000	Annual (15 Sep 99 - 14 Sep 00)

4. TITLE AND SUBTITLE
Automated Spot Mammography for Improved Imaging of Dense Breasts

5. FUNDING NUMBERS
DAMD17-99-1-9294

6. AUTHOR(S)
Mitchell M. Goodsitt, Ph.D.

7. PERFORMING ORGANIZATION NAME(S) AND ADDRESS(ES)
University of Michigan
Ann Arbor, Michigan 48109-1274

E-MAIL:
goodsitt@umich.edu

8. PERFORMING ORGANIZATION REPORT NUMBER

9. SPONSORING / MONITORING AGENCY NAME(S) AND ADDRESS(ES)
U.S. Army Medical Research and Materiel Command
Fort Detrick, Maryland 21702-5012

10. SPONSORING / MONITORING AGENCY REPORT NUMBER

11. SUPPLEMENTARY NOTES
This report contains colored photos

12a. DISTRIBUTION / AVAILABILITY STATEMENT
Approved for public release; distribution unlimited

12b. DISTRIBUTION CODE

13. ABSTRACT *(Maximum 200 Words)*

We are developing an automated spot mammography technique to improve imaging of lesions within dense breast tissue.

During the first year of this project, computer programs have been developed to identify large dense regions in digitized mammograms. The programs also determine the minimum sized rectangle that bounds a dense region. Prototype devices have been designed and built to: collimate the x-ray beam to the desired region, restrain the breast during changeover to a spot compression paddle, and manually translate the spot paddle to the desired location. Preliminary tests were also performed on a commercial full-field digital mammography (FFDM) system.

Sophisticated exposure control and technique factor selection on the FFDM improved the penetration of simulated dense regions in a breast phantom. Combined spot collimation and compression were found to increase lesion conspicuity with the FFDM. Rather than pursue research with our laboratory system, we have decided to build an add-on system for the FFDM, which has superior imaging properties. Initial experience with the prototype devices has indicated the need for design improvements. These will be implemented during the second year. Finally another improvement, the addition of stereo mammography to the auto spot procedure will be investigated.

14. SUBJECT TERMS
Breast Cancer

15. NUMBER OF PAGES
72

16. PRICE CODE

17. SECURITY CLASSIFICATION OF REPORT	18. SECURITY CLASSIFICATION OF THIS PAGE	19. SECURITY CLASSIFICATION OF ABSTRACT	20. LIMITATION OF ABSTRACT
Unclassified	Unclassified	Unclassified	Unlimited

NSN 7540-01-280-5500

Standard Form 298 (Rev. 2-89)
Prescribed by ANSI Std. Z39-18
298-102

(3) TABLE OF CONTENTS

(4) INTRODUCTION

The purpose of our project is to develop a novel technique for improved imaging of dense tissue regions with digital mammography systems. The basic idea is to automatically detect any large dense region within a whole breast digital mammogram, and to take a second digital mammogram of only that region using automated collimation and automated spot compression along with a more penetrating exposure. This second separate "spot mammogram" is taken within seconds of the full-field mammogram while the breast is maintained in the same position by a specially designed device that also allows additional compression by a spot paddle. Since only the dense region is exposed, detector saturation will not be an issue. Both restriction of the x-ray beam to a small area and compression of the tissue to a thinner thickness will decrease the volume of tissue that scatters x-rays thereby improving the contrast between lesions and surrounding dense breast tissue. Tissue differentiation will also be improved because of the increased separation of overlaying structures as a result of the spot compression. Furthermore, in comparison with conventional spot compression, the automated technique should produce more accurate compression of suspicious regions because it eliminates the need for the repositioning of the breast between the full-field and spot images, and the "spot" location is determined by computer analysis of the digital full-breast image rather than estimated by eye from a radiograph. In brief, the project entails development of software to analyze digital mammograms and automatically delineate suspicious dense tissue regions, and the development of hardware to automatically collimate the x-ray beam to those regions and to enable spot compression of those regions while maintaining the breast in the same position as for the original full-breast digital mammogram.

(5) BODY

During the first year of this project (September 1, 1999 - August 31, 2000), the following was accomplished relative to the tasks in the approved statement of work.

A) Develop software to recognize and delineate dense breast regions in full-breast mammograms.

Much work was devoted towards developing software that would automatically locate substantial dense breast regions in digitized mammograms. Two major programs to assist in accomplishing this task were produced. Both were written in Visual C++, which permitted the development of intuitive, user-friendly graphical interfaces for future studies in which radiologists will employ the programs to set gray level thresholds to isolate suspicious regions and will draw boundaries of the suspicious regions. The manual segmentation may serve as a gold standard for verification of the accuracy of the automated dense region detection program, and if the automated computer segmentation is not satisfactory for a give mammogram, manual correction will be allowed before activating the autospot collimation and compression. A database of 304 digitized dense breast images was generated for the programs by digitizing clinical mammograms that were classified as BIRADS 3 and 4 density by an MQSA-approved radiologist. Detailed descriptions of the major computer programs follows:

1) SEGNEW Computer Program

SEGNEW is a computer program that determines dense tissue regions in a mammogram. The operation of this program can best be explained by referring to its graphics display window as shown in Figure 1.

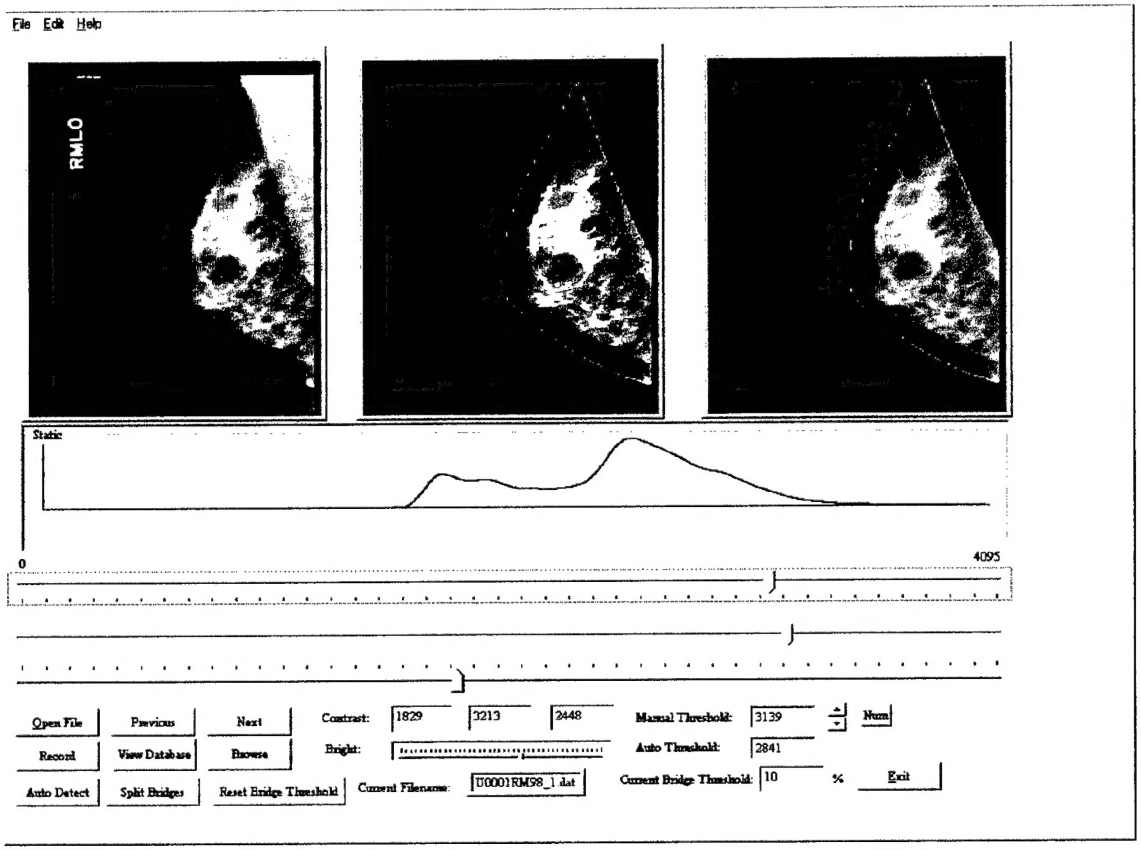

Figure 1: SEGNEW Display Window

1. Three versions of the digitized mammogram are displayed side by side at the top of the screen. The leftmost version is the original mammogram that has been modified by unsharp masking and software equalization to better display the breast periphery. The center mammogram shows the same mammogram with white lines delineating the computed breast boundary and pectoral muscle area (if present), and yellow painted pixels representing automatically detected dense tissue. The breast border is determined using a modified version of a routine we previously developed for a method to equalize exposures in mammography [1,2] that was also supported by a USAMRMC grant [No. DAMD 17-94-J-4292]. The methods for detecting the pectoral muscle and for determining an automated threshold for discriminating dense breast tissue were described by our group in a paper that was recently submitted for publication in Medical Physics [3]. The dense breast tissue discrimination is achieved using a rule-based technique, which determines the threshold from the shape of a smoothed amplitude histogram of the pixel gray-levels within the breast tissue region excluding the pectoral muscle. The same amplitude histogram is displayed beneath the 3 versions of the mammogram in Figure 1. Beneath this histogram are 3 sliders. The top slider is used to set a manual dense tissue

threshold. All pixels in the rightmost displayed mammogram that have gray levels greater than the manual threshold are painted yellow in the image, while the others retain their original gray levels. The radiologists will adjust the slider to find a threshold that results in yellow areas that best depict areas in the leftmost mammogram that they believe are candidates for spot mammography. It is important to note that the automatic threshold that is employed for the center image is chosen to differentiate all of the dense tissue; whereas, the manual threshold only selects the subset of the dense tissue that is suspicious and in need of spot imaging. To assist the radiologists in their assessments of the images, a contrast enhancement tool is provided. Contrast enhancement is achieved by adjusting the 2 lower sliders. The middle slider sets the minimum pixel value and the bottom slider sets the maximum pixel value in the original image that are transformed to the 256 gray levels in the output image. As the sliders are adjusted, the contrast and brightness of the image change. Once the radiologists are satisfied with their manual threshold settings, they press the record button, which causes the automatic and manual thresholds to be stored in a database. The differences between the automatic and manual thresholds and the ratios of the thresholds are computed in this database. In a future study we will evaluate the differences and ratios to determine if a statistically significant relationship exists that could be used to compute the appropriate manual threshold. The SEGNEW program also incorporates a software routine that determines the three largest dense tissue regions in the manually thresholded image. These regions are defined as being composed of contiguous pixels that have gray level values above the manual threshold. The program is invoked by pressing the "Auto-Detect" button at the bottom left corner of the display window. The program paints the largest dense region red, the second largest green, and the third largest blue. The result is displayed in the rightmost mammogram (See Figure 2, below)

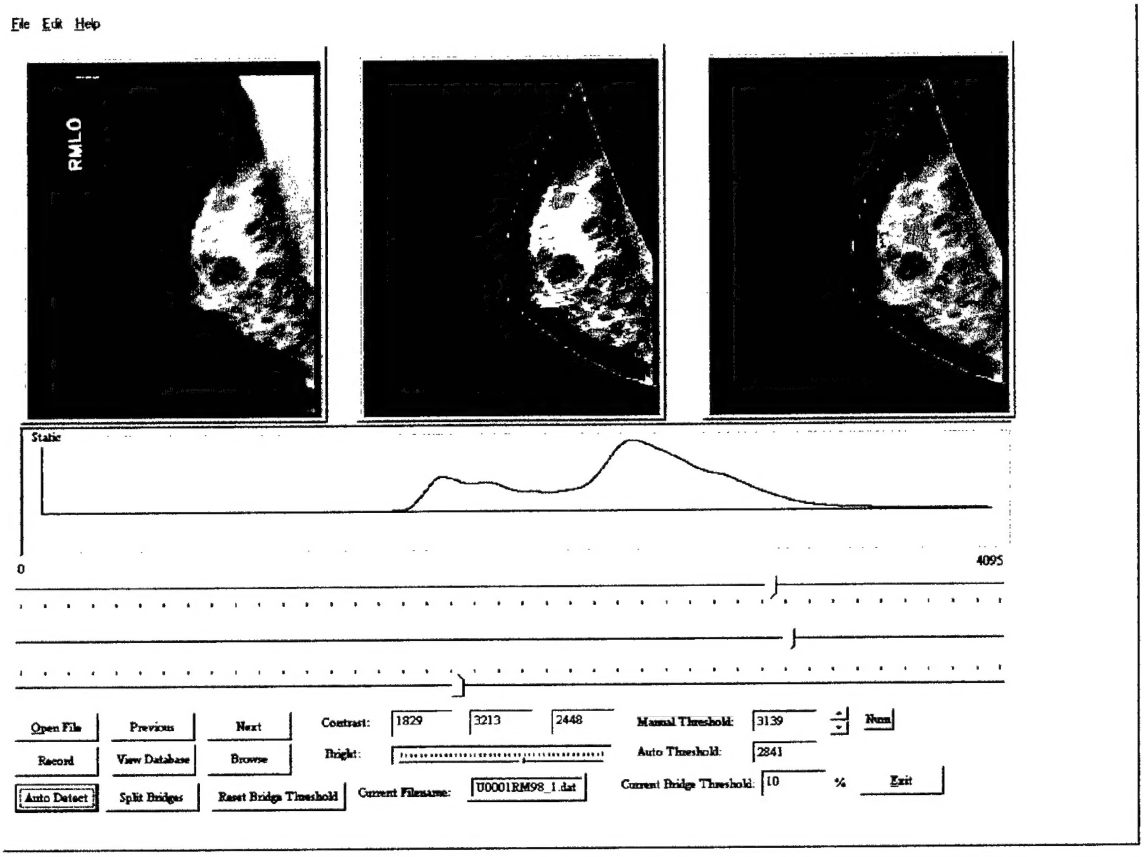

Figure 2: Example of routine that finds 3 largest dense tissue regions. These areas are indicated with the red, green and blue pixels in the rightmost mammogram.

Sometimes the dense regions contain areas that are connected by thin "bridges". Often it is appropriate to break these bridges to further subdivide the regions and better discriminate the three largest regions. A subroutine was written to detect and break such bridges. It is invoked by pressing the "Split Bridges" button on the window. This routine permits the user to select a threshold bridge width. This threshold is set to a percentage of the mean width of the region in a particular direction. Any bridge pixels that are less than this threshold width are cut out from the contiguous pixel region. The bridge pixels are searched for in the horizontal, vertical and diagonal directions. We have found a default bridge threshold of 10% appears to work well. This value may change in the future based on further radiologist evaluations. The rightmost mammogram in Figure 3 shows an example of the 3 largest dense regions in a mammogram as determined by the SEGNEW program, and Figure 4 shows the results of the "Split Bridges" routine when it was applied to the rightmost image in Figure 3.

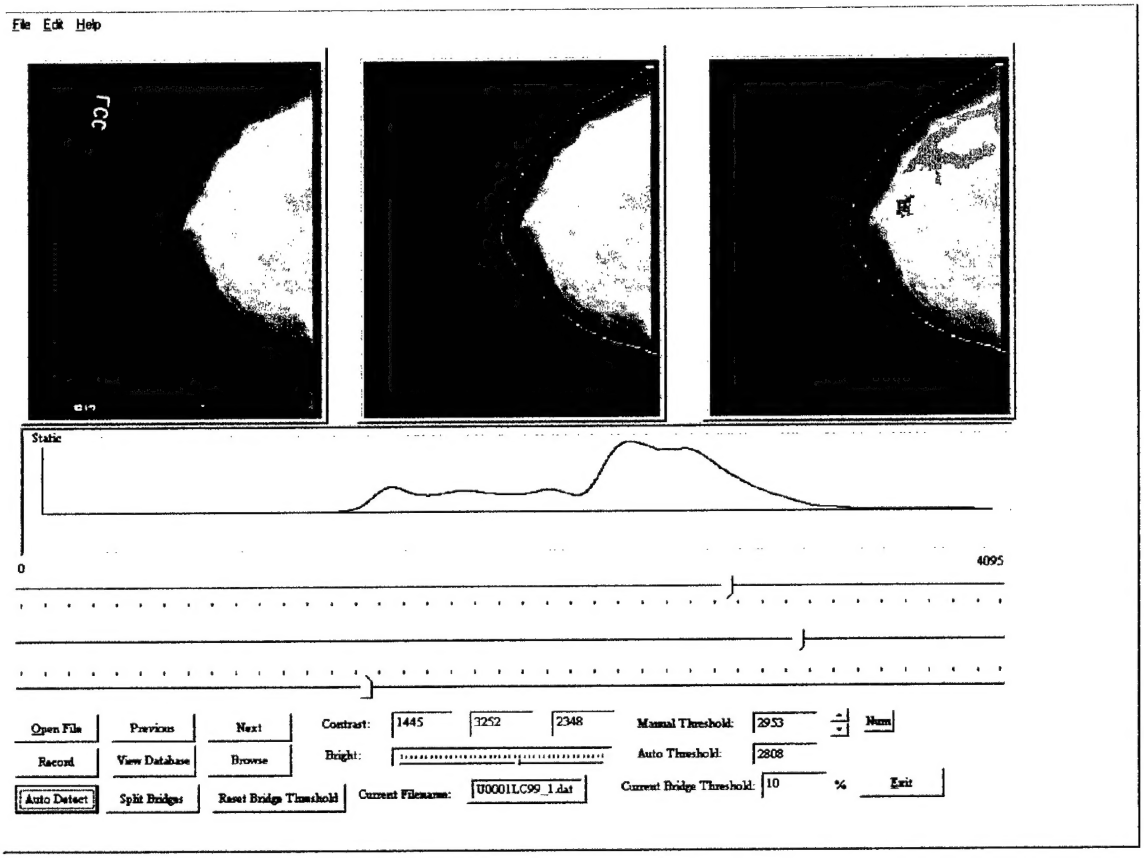

Figure 3: CC mammogram with three largest determined dense regions shown at right.

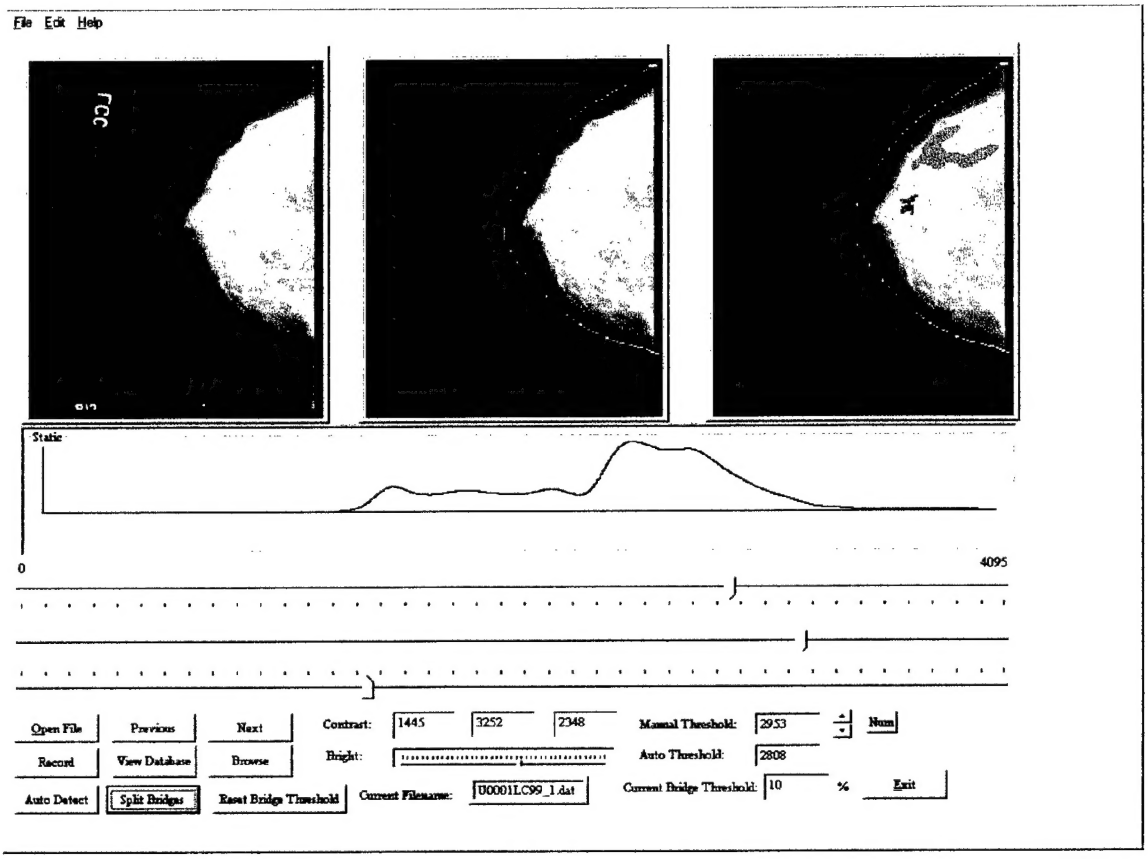

Figure 4: Same mammogram as in Figure 3 after application of "Split Bridges" routine. Note the large red region in Figure 3 is now partitioned into two regions (red and green).

2) DENSETEST Computer Program

Another method to demarcate suspicious dense regions in mammograms is to have the radiologists hand-draw boundaries around the regions. DENSETEST is a program that was written with this goal. The user can trace a suspicious region using the computer mouse. The trace consists of connected segments whose anchor points are generated by clicks of the leftmost mouse button. Thus, the user can control the fineness of detail of the outline. A high-detail outline is created using many mouse clicks as the outline is drawn, and a low-detail outline is generated using very few mouse clicks. When in the course of drawing the outline, the trace approaches the starting point, the program automatically completes the connection to the starting point and the outline is finished. After this, the user can adjust the outline by grabbing any of the anchor points and pulling them to a new position. The outline is stored when the user presses the "NEXT" button in the display window. DENSETEST also computes the minimum sized rectangle which bounds the final traced border of the suspicious region. This rectangle corresponds with the collimated region in a 4-collimator blade implementation of automated spot collimation. The algorithm computes the minimum sized rectangle by an iterative approach similar to that described in the original proposal. That is, first, the center of mass of the dense region is located. Next, perpendicular x- and y- axes are drawn through the center of mass. The dense tissue pixels having maximum and minimum x and y coordinates relative to these axes are determined. Lines perpendicular to the axes passing through these points define the rectangle. The area of this rectangle is computed.

Next, the axes are rotated by 1-degree increments, and the bounding rectangle and the rectangle areas are computed. The rectangle with the smallest area is selected. Example of the display window with traced borders (in red) and minimum sized bounding rectangles (in green) are shown in Figure 5A and B, below.

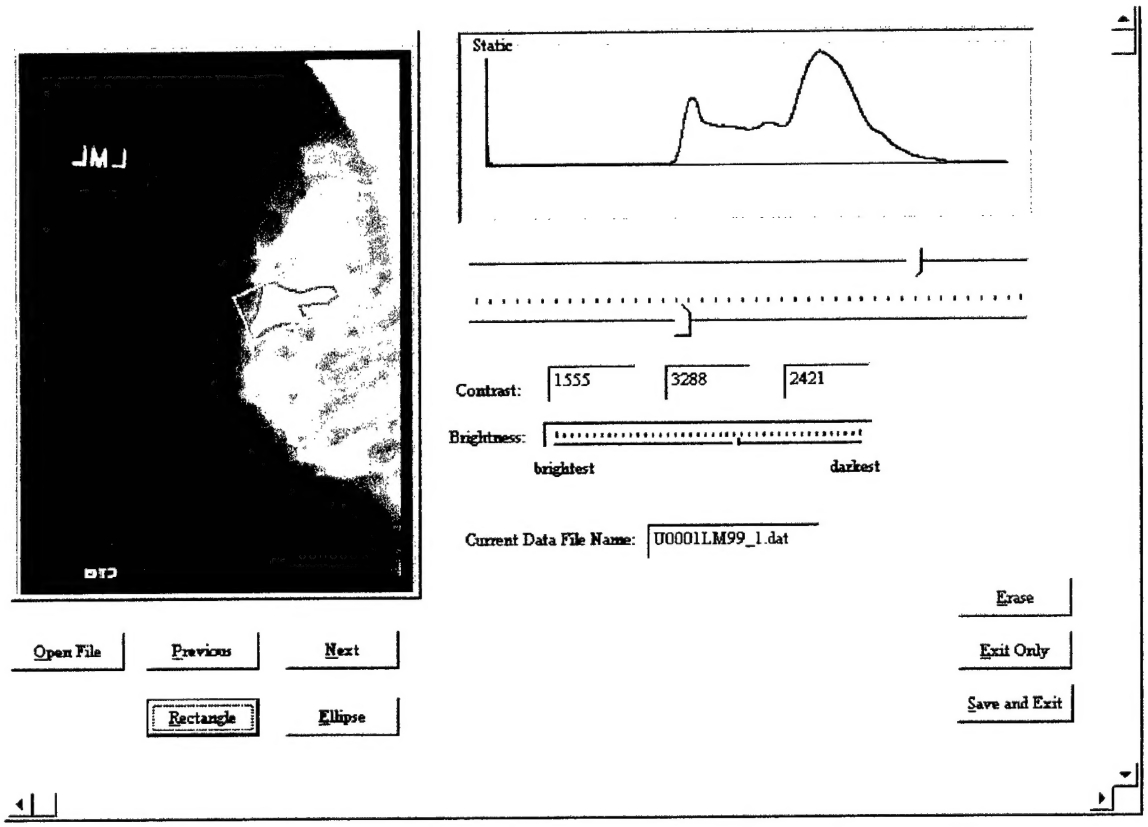

Figure 5A

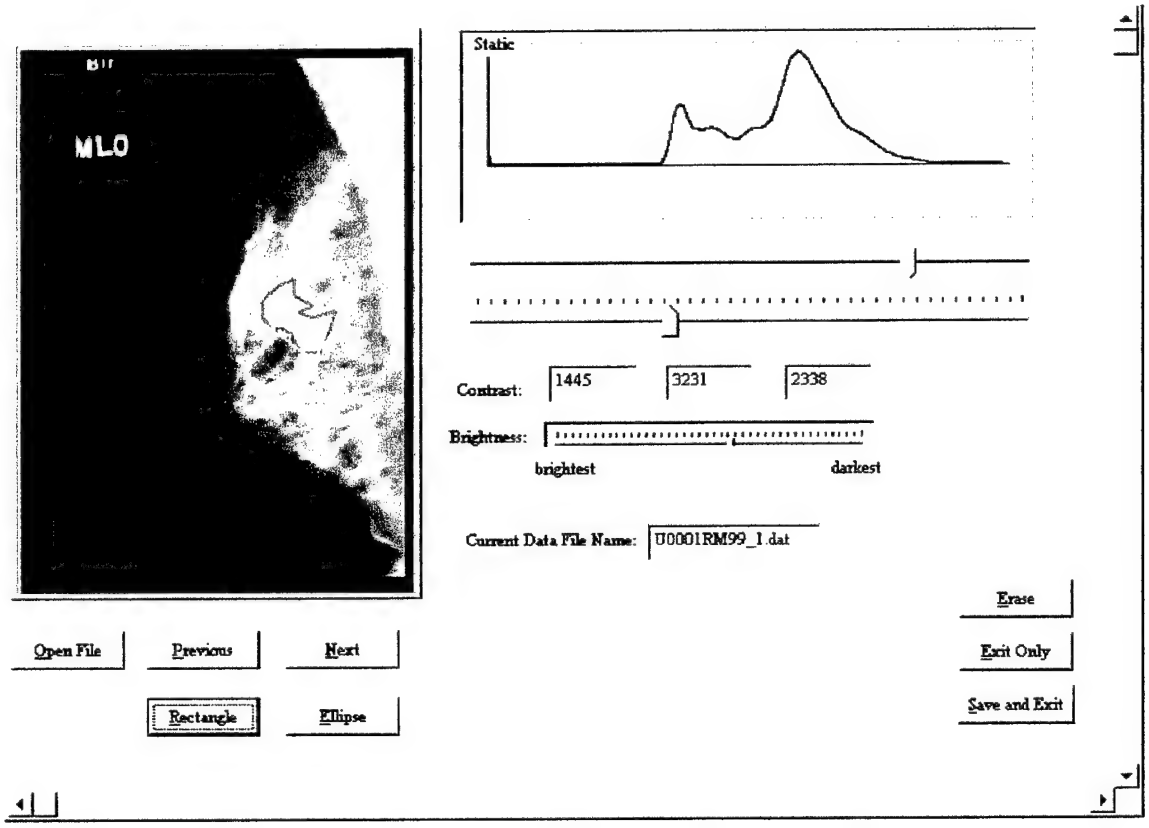

Figure 5B

Figure 5 A and B: Two examples of traced suspicious dense tissue regions (in red) and the corresponding computed minimum sized rectangles (in green) delineating the collimated area for automated spot mammography

Notice in Figure 5 that the DENSETEST program permits the user to adjust the contrast and brightness of the image with slider controls similar to those employed in the SEGTEST program described above. Also, there is a button labeled "Ellipse". This button initiates a routine that computes the minimum sized ellipse bounding the traced border. This will allow us to investigate the use of elliptically shaped collimator blades. It presently is a works -in-progress.

Elliptical Collimation

The advantage of an elliptical collimator is that two blades could be used to restrict the beam rather than 4, which are required for rectangular collimation. This would also simplify the mechanics of the system since only 2 stepper motors would be required for collimator blade translation rather than 4 for rectangular collimation. A potential disadvantage of elliptical collimation is that the aperture shapes that can be achieved are more restricted and therefore the degree of collimation may be significantly less than what can be achieved with rectangular collimation. Thus, more "normal " tissue would have to be exposed in some cases with elliptical collimation. Investigations are planned to determine the adequacy of elliptical collimation. Outlines of dense breast regions created by radiologists using the DENSETEST program will be

fit with ellipses. An average elliptical curve will be computed, and the collimation accuracy that can be obtained with this shape will be compared with that which can be achieved with rectangular collimation. One measure of collimation accuracy will be the ratio of the area of the ellipse or rectangle to the area of the freehand outlined region. If the average elliptical curve does not work well, other arc shapes will be tried. This investigation is not described in the original proposal. It is a new idea that we conceived while working with mechanical engineering students building a prototype asymmetric collimator for the project (See below). The investigation of arched or elliptical shaped collimator blades will be performed during the second year of the project.

Radiologist's review of programs and planned changes

The Radiologist who is working with us on this project reviewed the computer programs. In general, he found them to be satisfactory. He did suggest that we modify the DENSETEST program to permit the radiologists to outline the 3 most suspicious regions rather than just one. He also told us he would prefer that the collimation not be as tight as initially planned. He would prefer an additional 1-cm margin around the entire boundary so more of the breast architecture would be seen in the spot compression image. We are implementing these changes. We will also investigate just using the resulting outlines with the DENSETEST program to determine the gray level threshold in the SEGNEW program. Should a simple threshold not work, we will investigate other means for defining the suspicious dense region such as use of textural and morphometric features.

B) Develop secondary collimator

Working in conjunction with 5 senior mechanical engineering students at the University of Michigan, we designed and built a prototype collimator. This collimator was designed to be attached to the aperture holder of the Fischer MammoVision biopsy system in our lab. Various design options were explored including an "elevator door" (4-blade) system which produces asymmetric rectangular collimation, a two L-shaped plate collimator, an actuator rod system with two rods attached to each collimator blade to translate and angle the blade, a two blade collimator with arched ('C'-shaped) openings, and a 4-blade collimator that employs a splined shaft gear selector clutch system which enables driving 2 plates, one at a time with a single motor. The system consisting of two blade collimators with arched ('C'-shaped) openings was chosen because it was the least complex, requiring fewer stepper motors and controllers. The system that was built consists of two 2 mm thick arch shaped steel plate collimator blades ("doors") that are translated back and forth by stepper motors via rack and pinion drives. The entire assembly is mounted to an aluminum plate, which has a "lazy susan" bearing to permit rotation. Rotation is achieved via a worm and roller connection to a third stepper motor. A CAD drawing of the prototype is shown in figure 6A, and a photo of the final unit is shown in figure 6B, below.

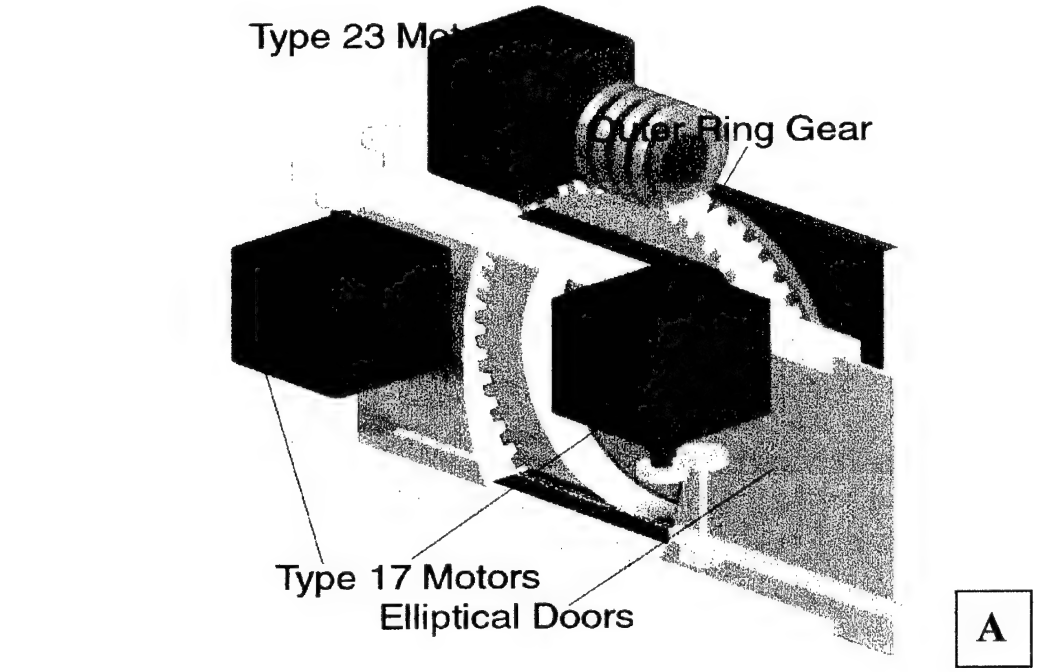

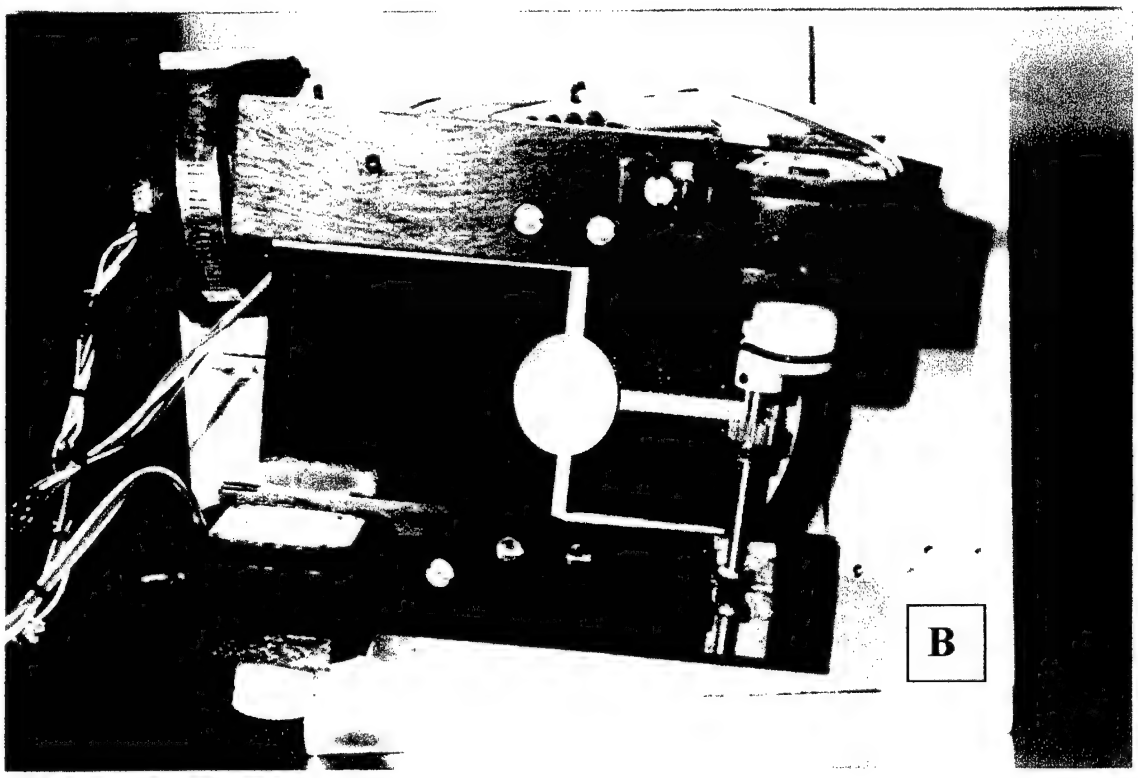

Figure 6. CAD drawing of prototype automatic collimator (A) and photo of finished product (B). (The elliptical collimator blades are shown in a fully open position in (B).)

The composition and thickness of the collimator blades was decided upon based on x-ray transmission calculations for a variety of metals. Metals that were investigated included lead (Pb; ρ=11.36 g/cm^3), steel (99% Fe, 1% C; ρ=7.83 g/cm^3), tin (Sn; ρ=7.3 g/cm^3), tungsten (W; ρ=19.3 g/cm^3) and tantalum (Ta; ρ=16.6 g/cm^3). The goal was to find a metal that was very attenuating, light weight, and easy to machine. X-ray attenuation coefficients were employed from Tables in The Physics of Radiology by Johns and Cunningham [4] and from the Saloman and Hubbell [5]. Examples of the results for various thicknesses of the metals are shown in Table 1, below:

Table 1: X-ray Transmissions of Various Metals

		Fraction transmitted at 20 keV					Fraction transmitted at 30 keV				
Thickness inches	Thickness mm	Pb	Steel	Tin	W	Ta	Pb	Steel	Tin	W	Ta
1/64	0.4	1.51 E-17	3.97 E-04	2.04 E-03	5.15 E-23	2.71 E-18	1.51 E-06	8.20 E-02	6.80 E-06	2.23 E-08	1.19 E-06
1/32	0.8	2.28 E-34	1.58 E-07	4.16 E-06	2.66 E-45	7.32 E-36	2.28 E-12	6.72 E-03	4.63 E-11	4.99 E-16	1.43 E-12
1/16	1.8	5.18 E-68	2.49 E-14	1.73 E-11	7.05 E-90	5.36 E-71	5.19 E-24	4.51 E-05	2.14 E-21	2.49 E-31	2.04 E-24
	2	1.70 E-85	7.27 E-18	2.76 E-14	4.82 E-113	2.95 E-89	4.62 E-30	3.35 E-06	9.11 E-27	2.78 E-39	1.42 E-30
1/8	3.2	2.69 E-135	6.20 E-28	2.99 E-22	4.97 E-179	2.87 E-141	2.69 E-47	2.04 E-09	4.58 E-42	6.18 E-62	4.16 E-48
3/8	6.4	7.23 E-270	3.84 E-55	8.91 E-44	0.00 E+00	8.26 E-282	7.26 E-94	4.14 E-18	2.10 E-83	3.82 E-123	1.73 E-95

The transmissions were calculated using the equation:

$$Transmission = e^{-(\mu/\rho)\rho t}$$

where (μ/ρ) is the mass attenuation coefficient in cm^2/g, ρ is the mass density in g/cm^3 and t is the thickness in cm. The transmissions were calculated at 20 keV which is approximately the effective energy of a conventional mammography x-ray beam spectrum and at 30 keV which at this time is greater than the maximum effective energy of the x-ray beams used in digital mammography. The areal densities of the metals were also computed in order to compare the masses of the various thicknesses of the metals. These are listed in Table 2, below.

Table 2: Areal Densities of the Metals (= ρt) (unit = g / cm^2)

Thickness (inches)	Thickness (mm)	Lead (Pb)	Steel	Tin (Sn)	Tungsten (W)	Tantalum (Ta)
1/64	0.4	0.45	0.31	0.29	0.77	0.66
1/32	0.8	0.90	0.62	0.58	1.53	1.32
1/16	1.8	1.80	1.24	1.16	3.06	2.64
	2	2.27	1.57	1.46	3.86	3.32
1/8	3.2	3.61	2.49	2.32	6.13	5.27
3/8	6.4	7.21	4.97	4.63	12.26	10.54

Also, with the aid of a service person, we opened the gantry cover of a GE DMR mammography system at our hospital and examined the collimator blades. They were found to be made of 2-mm thick steel plate. As can be seen from Table 1, the x-ray transmission through such a blade is 7 x 10^{-18} at 20 keV and 3 x 10^{-6} at 30 keV. From table 2, the weight of such a blade is 1.6 g/cm^2. Similar transmissions can be achieved with significantly less weight using 1/64" of either lead

(0.45 g/cm^2), tungsten (0.77 g/cm^2) or tantalum (0.66 g/cm^2). 1/16" of tin (1.16 g/cm^2) could also be used; however, tin has a K-absorption edge at 29.2 keV and will transmit larger amounts of x-rays just below this K-edge than other metals so it would not be an ideal choice. We decided to use 2-mm steel in our prototype because it provides adequate attenuation, is readily available, is easy to machine, and is inexpensive. The much lighter weights of lead, tungsten, and tantalum will be explored for the next collimator system that is built. The very thin thicknesses of these metals make them less rigid than 2 mm of steel, so they may need to be mounted on a thicker light- metal plate such as aluminum. The entire weight of the combined metals will be compared with that of steel alone and other factors including the ease of machining of the metals and availability and price will also be considered in making the final decision.

Based on torque requirements, NEMA # 17 motors ((20 oz-in. holding torque) were employed to translate the two collimator blades, and a NEMA #23 motor (50 oz-in, holding torque) was employed to rotate the assembly. The NEMA #17 stepper motors were driven with Mill Shaf Technologies (Yadkinville, NC) A-100 stepper motor controllers, and the NEMA #23 stepper motor were driven with a Mill Shaf Technologies A-200 stepper motor controller.

Tests were performed with the system, and it was found that the time to collimate was about 1 to 1.5 seconds depending upon the desired final positions of the collimator blades. This time would be adequate for patient studies. One major problem that was discovered was that the use of the simple stepper motor controllers limited the accuracy of collimation. For example, programming a motor to move 50 steps in the forward direction resulted in the translation of a collimator blade by approximately 0.5 inches; whereas, programming the same motor to move the 50 steps in the reverse direction resulted in a translation of only 0.3 inches. It appears that the motor skipped steps in the reverse direction. This could be corrected by using a more sophisticated and expensive closed-loop, proportional derivative integral controller with zero steady state error.

Improvements for future automated collimator system

From our initial experience with the prototype automated collimator system, the students derived the following list of improvements that they would recommend in future systems:

1) For patient safety and to reduce noise levels, a foam-lined shroud should be added to cover moving parts.
2) For reliability, a mechanical stop should be added to the ends of the tracks in order to prevent the collimator blades from falling out of the tracks if the racks should disengage from the pinions.
3) For smoother meshing of the worm drive with the gear, a support bearing should be added. The shaft of the drive would pass through this bearing to eliminate the present cantilever design, and the bearing would be secured to the aluminum plate for stability.
4) For faster rotation speeds with more compact mounting, the worm gear should be replaced by multiple spur gears.
5) To eliminate inaccuracies in collimator blade translation, use closed loop proportional integral derivative (PID) controllers with zero steady state error.
6) If angle accuracy is not super critical, consider using a smooth, quiet operating DC motor instead of a NEMA #23 stepper motor to rotate the apparatus.

We will implement many of these suggested changes in our next design.

C) Develop system to restrain breast during changeover from full-field to spot compression paddle and reduce tension as spot paddle presses against breast.

We worked with another 5 senior mechanical engineering students on the design and manufacture of a system to restrain the breast during the changeover from the full-field to the spot compression paddle and to reduce the tension as the spot paddle presses against the breast. This was a different group of students than that which worked with us on the automated collimator apparatus. This second group also worked with us on the spot paddle positioning system described in Section D, below.

Several designs for the breast restraining apparatus were considered. In one, a roll of Mylar was attached to one side of the breast support plate, and it was unrolled across the breast and attached to the other side of the plate. A ratcheting mechanism would be employed to tighten the Mylar membrane. In a second design, a Mylar membrane is stretched and held in place by a 'U' shaped frame. This frame translates on rails located at the bottom left and right corners. The frame is connected to the rails with sliders that include a ratcheted self-locking mechanism. This design called for the operator (i.e. the x-ray technologist) to release the lock on the sliders as the spot paddle compressed the breast. The second design, although not practical as a clinical device, was chosen because a prototype could be constructed easily to allow us to perform initial investigations. A drawing and photo of the apparatus appear in Figure 7.

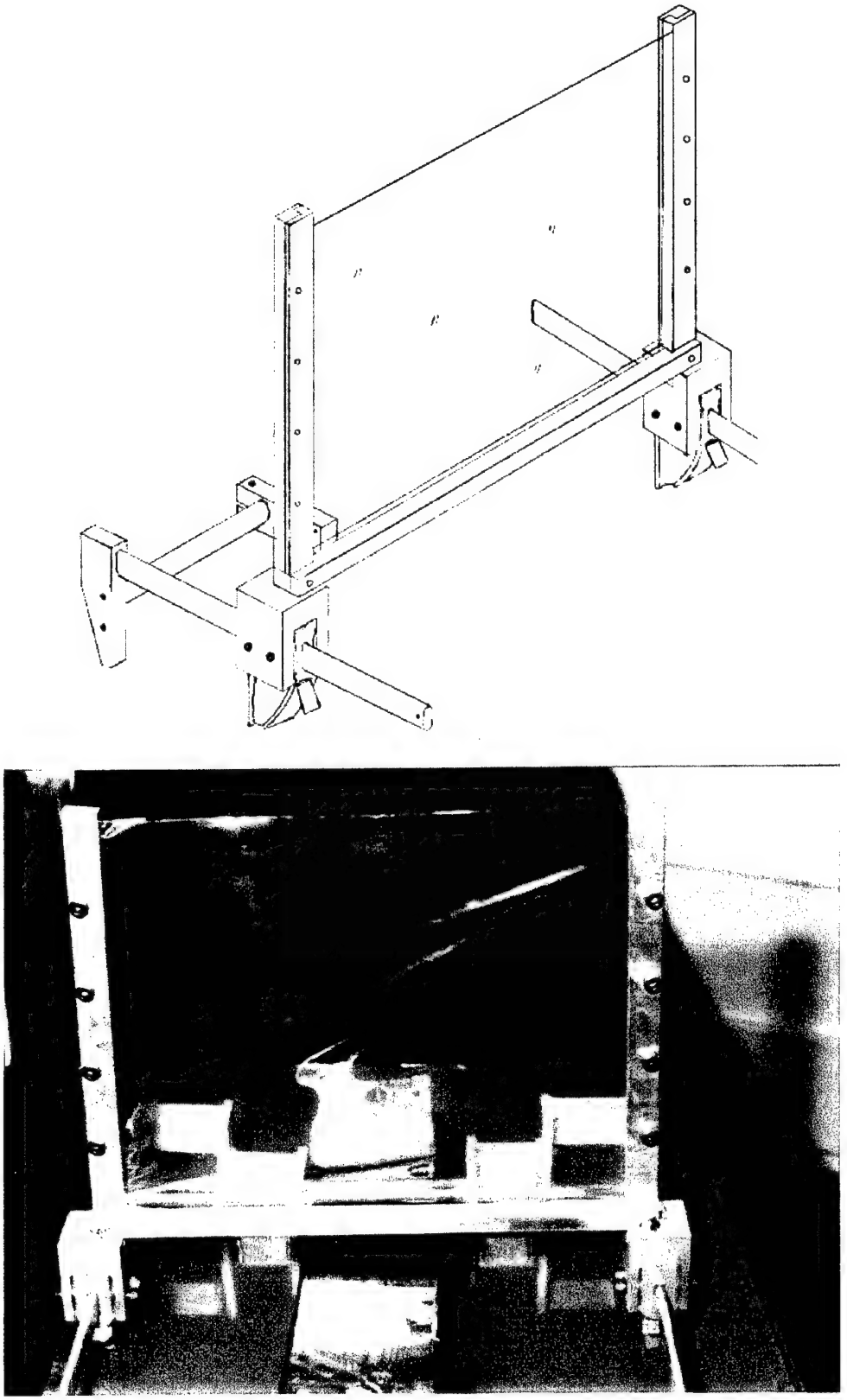

Fig. 7: Sketch (top) and photo (bottom) of breast restraining device.

In general, the prototype was found to be unsatisfactory. The 'U' frame was designed to hold the Mylar in place by pinching it between two metal plates, but this did not work well. The Mylar slipped out, wrinkled, and could not be held tight. Even passing screws through the frame into holes punched near the edges of the Mylar did not secure the Mylar adequately. The mechanism for locking the position of the frame on the rails was difficult and awkward to use. The handles on the locks were too short and it was hard to unlock the mechanism from both sides to translate the frame on the rails. A single rail at the bottom center of the 'U'-shaped frame would have been better, but this would have interfered with the translator for the primary compression paddle of the Fischer unit, which is located in this region. During the second year of this proposal, we will develop a more satisfactory breast restraining device based on design number 1 described above.

D) Develop system to position spot compression paddle.

Although the development of the system to position the spot compression paddle was not originally planned until the second year ("months 15-19"), we did accomplish this task during the first year. We worked with the same 5 senior year mechanical engineering students that worked on the breast-restraining device. In this case, the results were much more satisfactory. The goal was to develop a system to efficiently translate a spot compression paddle to the desired location for the acquisition of the automated spot compression image. A sketch detailing the parts of the translational device is shown in Figure 8, below.

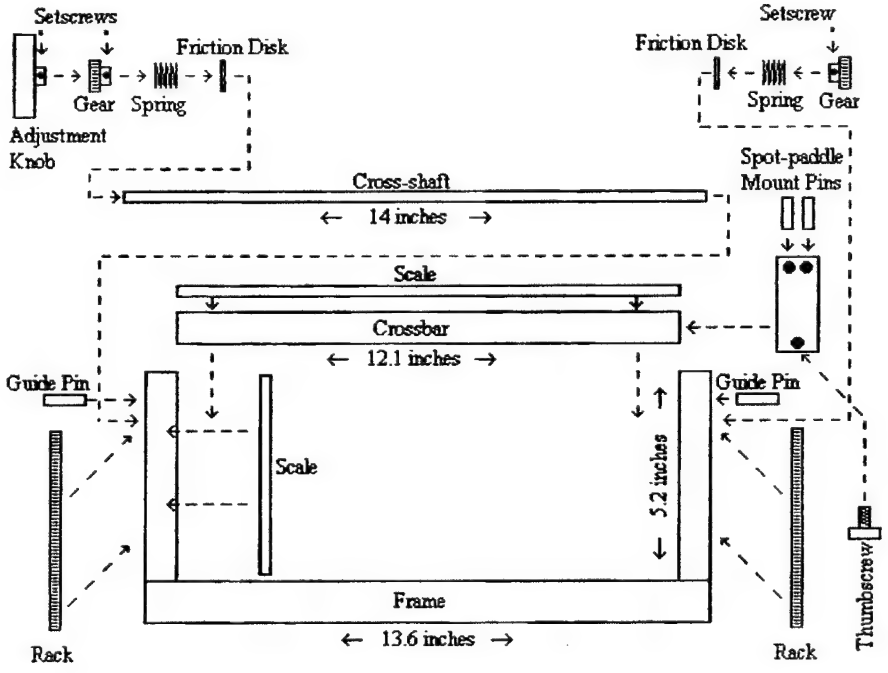

Figure 8: Exploded view of spot-paddle translation device.

A photo of the device attached to the Fischer MammoVision biopsy system is shown in Figure 9.

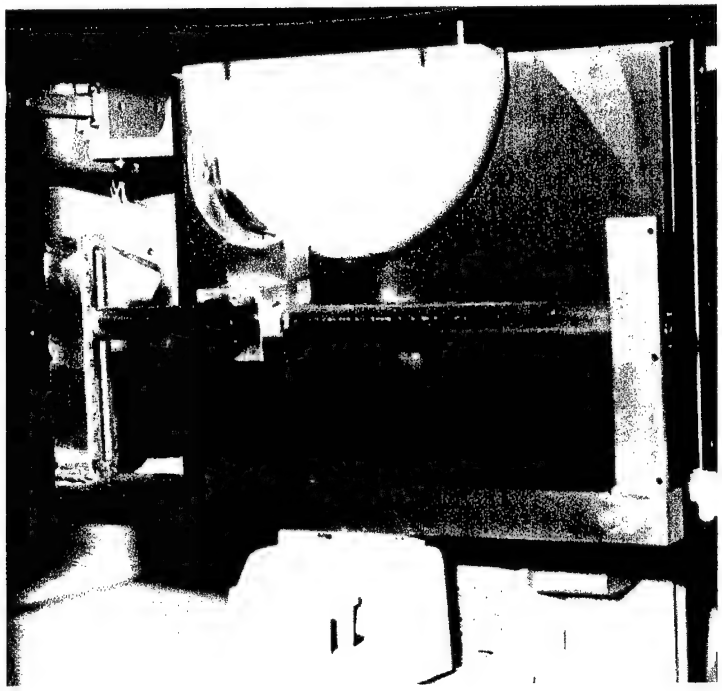

Figure 9: Photo of the spot compression paddle translation device in operation on the Fischer biopsy system. The plastic spot compression paddle is shown at an asymmetric position compressing a CIRS mammography phantom.

Note the paddle is positioned next to a CIRS breast phantom. The height of the paddle is adjusted by turning a knob that is connected to a horizontal cross-shaft containing two gears that travel along two vertical racks, one on each side of the device. The spring and disks on each side (Fig. 8) are used to maintain the vertical positions of the cross-shaft and crossbar. The steel guide pins slide along the slots and prevent the crossbar from twisting. The paddle mount was milled to slide along the crossbar and the cross-shaft. The paddle mount is secured in position with a thumbscrew. Metric scales are glued to the top of the crossbar and to the left upright. These scales enable the user to position the paddle to the nearest millimeter in the horizontal and vertical directions. Tests of the system showed it was able to compress with a force of 30 lbs., which was the intended design. We were also able to position the device from a remote starting position to a desired horizontal and vertical position with an accuracy of 1 mm in about 4 seconds, which is reasonable.

We did experience some problems with the translator. The crossbar guide pins had too much play, which allowed the crossbar to twist a small amount. Also, the slide mechanism for horizontal positioning of the spot paddle would sometimes bind. Our plans for building another translator

include machining to greater tolerances and the use of a rack and pinion system for horizontal as well as vertical positioning.

E) Develop prototype autospot system and evaluate with phantoms

In our original proposal, we planned to perform all of the autospot development on the Fischer MammoVision biopsy system we have in our lab. The reason was that that we had no digital mammography system at our hospital, and the biopsy system with radiography (CR) plates as the digital detectors was the most convenient system available for research. Just this past year, General Electric received FDA approval for clinical use of their Senographe 2000D full-field digital mammography (FFDM) system, and our hospital has purchased one. For the past two months, it has been temporarily housed in our research lab while the hospital renovates a clinical room. During this time, we have had a chance to perform some phantom experiments with the GE FFDM system. In one experiment, we added a simulated dense tissue and a simulated mass region to an experimental dual modality (x-ray and ultrasound) compressible breast phantom that we had manufactured for us by CIRS. A photo of the phantom with a blue dense region made of SMUD, a PlayDo-like compound made by Mattel (El Segundo, CA), and a yellow mass region made of Silly Putty (Binney and Smith, Inc. Easton, PA) is shown in Figure 10.

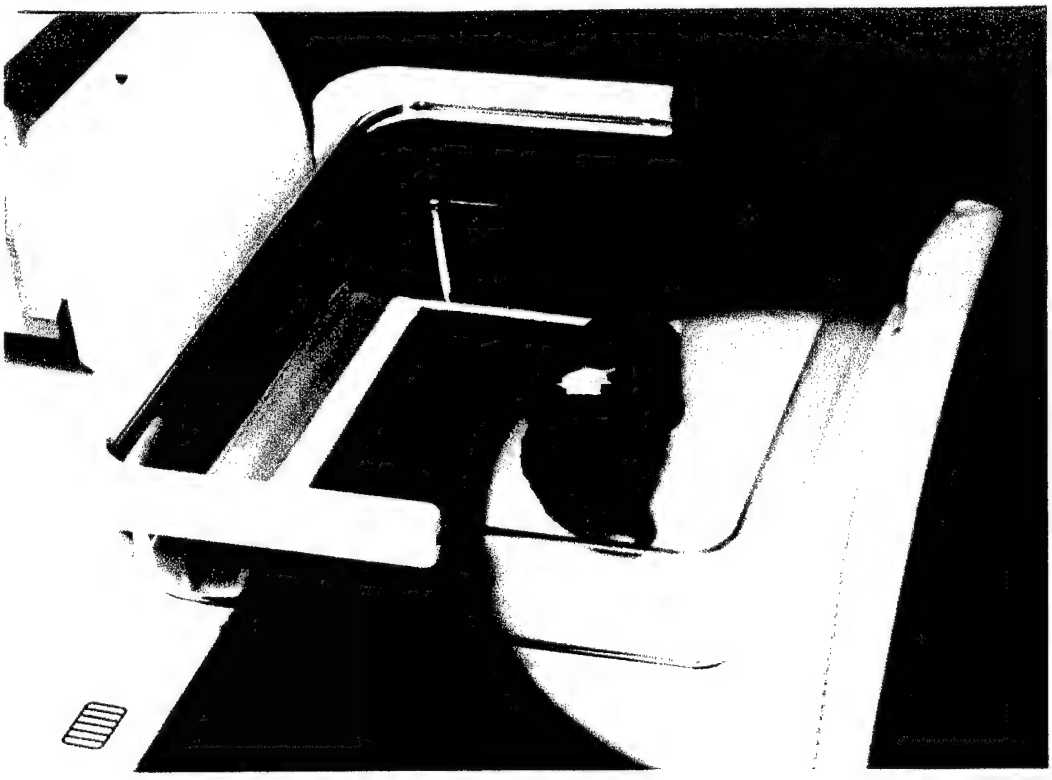

Figure 10: Compressible dual--modality CIRS breast phantom with superimposed simulated dense breast region (blue) and spiculated mass (yellow).

We then imaged the phantom with full field collimation, and with special collimation restricted to the dense tissue - mass region. The latter was achieved by taping strips of lead to the collimator port of the x-ray tube (See Figure 11).

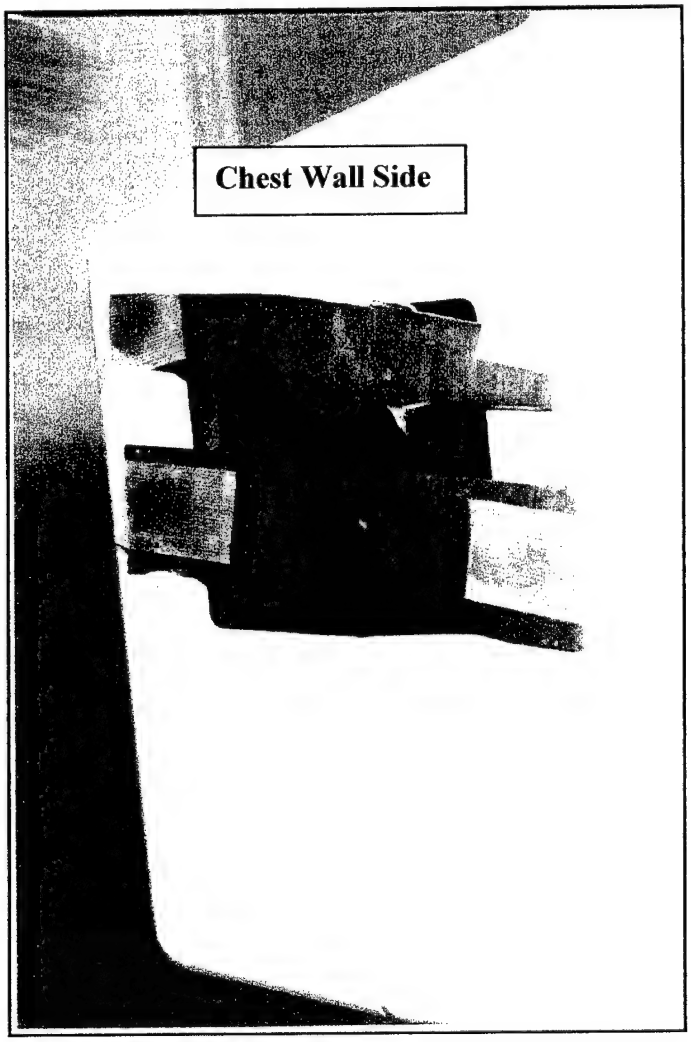

Figure 11: Handmade supplemental collimator used to restrict the x-ray beam to only the dense tissue - mass (blue/yellow) region in Figure 10.

The automatic exposure control (AEC) and automatic technique facilities (AOP) of the GE system were employed to generate both images. These are very sophisticated mechanisms. Based on a brief test-exposure, and compressed breast thickness information, the AOP automatically sets the x-ray tube target and filtration and kVp for optimal imaging in the given mode. These modes include CONTRAST AUTO in which the contrast is optimized using a lower effective x-ray beam energy, and a higher glandular x-ray dose than with the other techniques, STANDARD AUTO, which uses a higher x-ray beam energy to achieve a high quality image at less dose than in CONTRAST AUTO, and DOSE AUTO, which is optimized to produce a high quality image at a low glandular tissue dose. Our understanding of the operation of automatic exposure control of

this system from discussions with GE engineers is as follows. In contrast to conventional systems in which the phototimer of the AEC samples a small region of the breast at a technologist selected position to determine the exposure time, the GE FFDM system samples the entire image, and determines the exposure time from real-time sampled pixel values in the densest 1 cm x 1 cm region of the image. This sampling occurs in both the full-field and spot collimated images. Thus, in theory, the dense tissue should be adequately penetrated in both full-field and spot collimated images generated with the GE FFDM system. Our preliminary tests tend to confirm this. With appropriate adjustment of the window level and width to maximize the displayed contrasts of the full-field and spot collimated images of the phantom, we noticed very little difference between the two. A few subtle microcalcifications were visible in the spot collimated images and not in the full-field images, and the contrasts of some microcalcifications were better in the spot collimated image. However, in general, most of the image details (microcalcifications, simulated masses, etc.) were, on a subjective level, equally visible in both images. A quantitative analysis will be performed in future experiments to compare the contrast-detail in the images.

We also performed a second experiment in which we employed both spot compression and collimation. For this experiment, we employed a CIRS dual-modality phantom, and the middle sized spot compression paddle and spot collimator of the GE FFDM system. We did have to move the phantom to the region of interest for spot collimation, which would not be required with our proposed auto spot collimation/compression technique. The resulting full-field and spot images are shown in Figure 12, below. The white arrow in the spot image points to a mass that shifted positions when the spot compression was applied. This mass was hidden beneath another mass-like object in the full field image. This demonstrates a key advantage of spot compression, namely the spreading out of overlapping tissues for reduced superposition in projections and therefore improved imaging of lesions. Spot compression, however, may not always be successful in separating overlapping tissues. The degree of separation depends upon the position of the spot paddle relative to the tissues, the shearing forces placed by the spot compression paddle on the lesion and surrounding tissues, the tissue composition and architecture near the lesion, the sizes of the structures that are beneath and above the lesion as well as the size of the lesion itself. A better appreciation of the true nature of a suspicious object could be achieved by combining automated spot compression and collimation with 3D imaging (e.g., stereo mammography or tomosynthesis). The exploration of designing such a capability into a second generation automated spot system for human subject studies was a task mentioned in our original proposal.

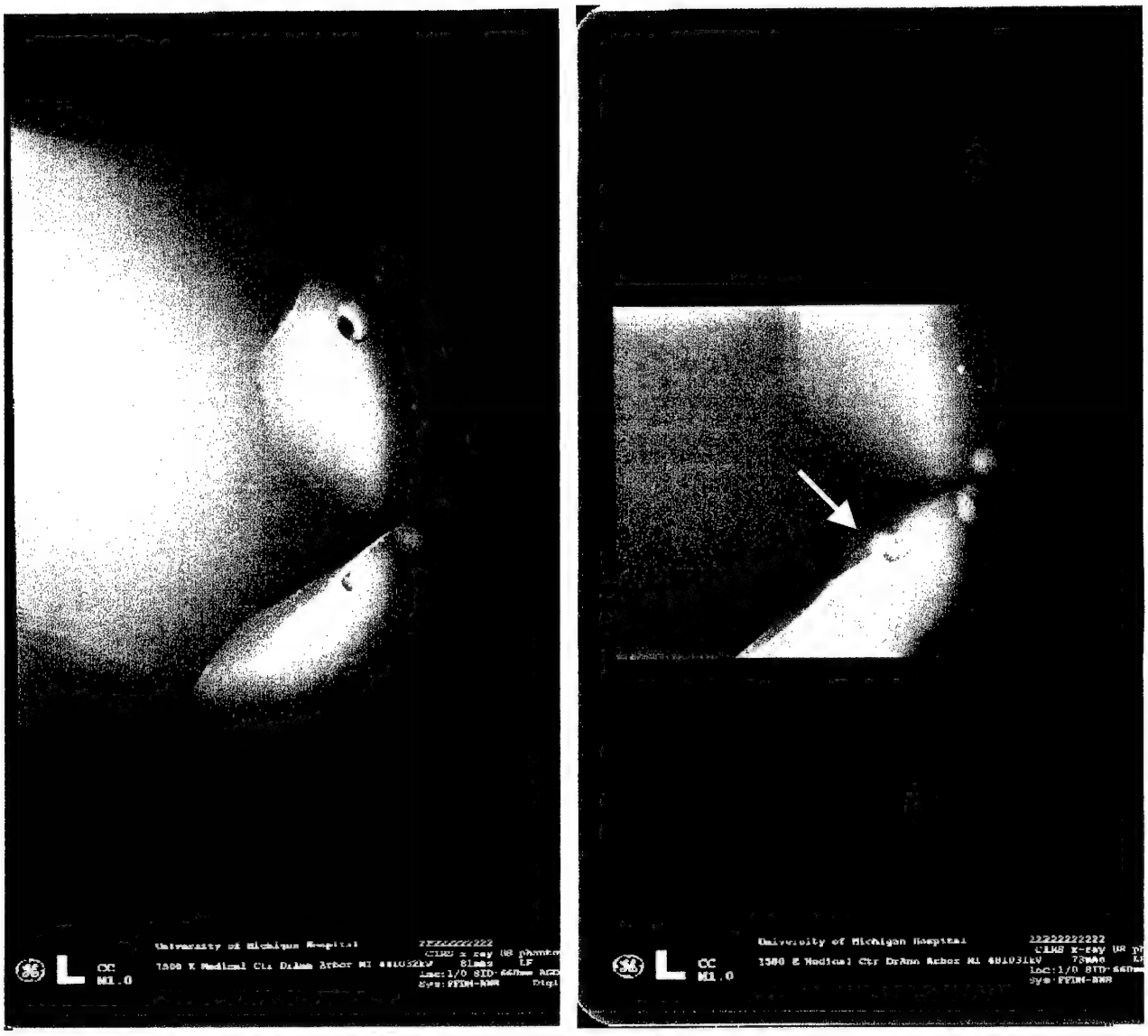

Figure 12. Full-field (left) and spot compression (right) images of a compressible breast phantom produced with a GE digital mammography system. The arrow in the right image points to a simulated mass that, due to spot compression, was separated from overlapping with another object, resulting in improved conspicuity of the mass.

F) Changes in Tasks for Second Year

Our preliminary studies with the full field digital mammography (FFDM) system that our hospital recently purchased indicate it would be the ideal test bed for developing the automated spot collimation/compression system. It was our eventual goal to adapt a system that we developed with the x-ray biopsy system in our laboratory and CR plate detector to such a full field digital mammography system. Although the full field digital mammography system will not be as convenient to use for research since it will be in the clinic and not our laboratory, we still can use

it during off hours. Advantages to developing an add-on automated spot system for the full-field digital mammo unit far outweigh the inconvenience issue cited above. These advantages relative to the biopsy/CR system include: the superior quantum detection efficiency and therefore superior image quality of the digital detector, the much faster readout time for this detector, the very sophisticated automatic exposure control and automated technique factor selection of the unit for optimized imaging in both full-field and spot modes, and the use of more conventional upright instead of prone positioning for patient imaging. We have therefore decided to develop the automated spot system as an add-on to the GE Senographe 2000D full field digital mammography system. The spot collimator, spot paddle positioner, and breast restraining devices that were designed and manufactured during the first year of the project were prototypes that were to be redesigned and manufactured based on our initial experiences (see above). They all can be readily adapted to the GE Senographe 2000D. In addition, this FFDM with its fixed digital detector with rapid image readout is more ideal for developing spot stereomammography, and will afford us the opportunity to pursue this capability at an earlier stage (i.e. the second year) and to a greater depth than was originally planned in the project. Our initial studies indicate this feature may potentially be as important as spot collimation and spot compression. In summary, the primary changes for the second year of research will be to adapt the automated spot collimation and compression device to the GE Senographe 2000D FFDM instead of the laboratory biopsy /CR plate system, and to develop spot stereomammography with the FFDM system.

(6) KEY RESEARCH ACCOMPLISHMENTS

- Acquired a database of 304 digitized dense breast images for computer analysis.
- Developed a computer program that permits the user to select a gray level threshold for segmenting suspicious dense breast tissue regions in digitized mammograms. Program also automatically determines 3 largest dense tissue regions.
- Developed a computer program that enables users to trace borders of suspicious dense regions in digitized mammograms. This program also computes the smallest rectangular region that bounds the traced border. The rectangle corresponds with the positions of collimator blades for automated collimation to the dense breast region of interest.
- Designed and built a prototype secondary collimator for achieving automated spot collimation with the biopsy x-ray system.
- Designed and built a prototype device for restraining the breast during the changeover from the full-field compression paddle to the spot compression paddle.
- Designed and built a prototype x-y translation device for manually positioning the spot compression paddle at a desired location.
- Performed spot collimation experiment with compressible breast phantom on a GE full-field digital mammography system and evaluated degree of improvement afforded by spot collimation alone on such a system.
- Performed spot collimation and compression experiment with a compressible breast phantom on the GE full-field digital mammography system and evaluated improvement due to the combined spot collimation and compression.

(7) REPORTABLE OUTCOMES

Manuscripts

Zhou C, Chan HP, Petrick N, Helvie MA, Goodsitt MM, Sahiner B, Hadjiiski LM. Computerized image analysis: Estimation of breast density on mammograms. Medical Physics (submitted)

Abstracts and Presentations

Goodsitt MM, Chan HP, Huang H, Zhou C. Automated spot mammography for improved imaging of dense breasts. Accepted for presentation at the 86th Scientific Assembly and Annual Meeting of the Radiological Society of North America in Chicago, IL, November 26-December 1, 2000 (Abstract to be published in Radiology)

(8) CONCLUSIONS

Much groundbreaking work towards the development of a practical automated spot collimation and compression system has been performed during the first year of this project. Computer programs with user-friendly graphics interfaces have been developed to: 1) enable manual outlining of suspicious dense breast regions in digitized mammograms, 2) compute rectangular collimator blade positions for automated spot collimation to the outlined suspicious regions, and 3) set manual gray level thresholds for the determination of the suspicious regions. A radiologist has reviewed these programs and recommended changes for the full study that will be conducted during the second year of the project. Prototypes of a secondary spot collimator, breast-restraining device, and spot collimator positioner have been designed, built, and evaluated. The knowledge gained will be used to design and build improved devices during the second year of the project. The unanticipated purchase by our hospital of a clinical full-field digital mammography system has afforded us the opportunity to evaluate the automated spot collimation and compression concept on a state-of-the-art x-ray mammography unit. Preliminary tests with this system involving imaging compressible breast phantoms indicate the improvement in image quality afforded by spot collimation alone may be less than anticipated when a wide-dynamic range digital detector is used; however, the improvement for combined spot collimation and compression can be significant. These are subjective assessments on a very limited set of simulated cases. Additional quantitative studies will be performed to further evaluate these effects. The full-field digital mammography system has many advantages over the biopsy CR detector system that was originally planned for our project including greater quantum detection efficiency for superior image quality, faster image readout, and more optimum exposures through the use of sophisticated phototiming and automated x-ray technique factor selection. We believe adapting our automated spot collimation / compression technique to the FFDM will provide us with a head start in assessing the true capabilities of this method. We have therefore changed our plans and will develop an add-on automated spot collimation system for the FFDM rather than the biopsy/CR system. Devices to accomplish this task will be designed and manufactured during the second year of this project. The FFDM is also an excellent platform for developing spot stereomammography. Stereomammography allows viewers to visualize the 3-D nature of the breast tissue, thereby enabling them to better appreciate the true nature of the structures. Overlapping tissues appear separated, the borders of lesions are better demarcated, and the

positions of lesions and microcalcifications are better realized. We have been investigating the capabilities of digital stereomammography in another project funded by the U.S. Army Medical Research and Materiel Command (Grant No. DAMD 17-98-1-8210). Adapting this technique to spot mammography is a logical offshoot of this work. The availability of the FFDM makes the development of a practical stereomammography spot system possible earlier than had been anticipated in our original study design. We have therefore decided to pursue this development one year ahead of schedule, starting in the second year rather than the third.

So What

A key limitation of conventional x-ray mammography is the inability to optimally image regions of dense tissue. The new full-field digital mammography systems may reduce but not eliminate this problem. We recently have had the opportunity to perform preliminary tests with such a unit. This unit employs a digital detector that has improved quantum detection efficiency and a more linear response than film-screen, both of which result in better imaging of dense tissue. In addition it utilizes a very sophisticated phototiming method that determines the exposure time and the x-ray technique factors from the signals detected in the densest region of the image, which improve dense tissue penetration. Still, the imaging of lesions in dense tissues with such systems will not be completely optimal. The system we are developing adds 3 features that will further optimize the imaging of such lesions. First, there will be automated collimation to the dense region. This will reduce the amount of x-ray scatter that strikes the detector thereby reducing image noise. It should also restrict the region in which the automated technique and phototiming is determined, which may improve the penetration of this region. Second, there will be automated spot compression in the dense region. This will reduce the thickness of the tissue x-rayed, which reduces x-ray scatter and reduces x-ray beam hardening, both of which should improve the contrast in the image. In addition, spot compression causes tissues to spread out, which may separate the lesion from overlapping tissues, thereby improving the conspicuity of the lesion. Third, spot stereomammography can be performed in the dense region. This will produce a 3-D image of the lesion allowing the viewer to see a separation between lesions and overlapping tissues even if spot compression did not fully accomplish this task. It also permits improved visualization of the locations of lesions and microcalcifications and of lesion borders, all of which are important to the radiologists in making their diagnoses. Finally, all of the techniques are performed with the breast restrained to be in the same location as in the full-field mammogram, eliminating the guesswork associated with breast re-positioning in conventional spot compression mammography. Thus, in theory, the automated spot collimation, compression, stereomammography technique should be of great benefit. The challenge will be to develop a convenient and practical system, which is the goal of our project.

(9) REFERENCES

1) Morton AR, Chan HP, Goodsitt MM. Automated model-guided breast segmentation algorithm. Medical Physics 1996; 23: 1107-1108.

2) Goodsitt MM, Chan HP, Liu B, Guru SV, Morton AR, Keshavmurthy S, and Petrick N. Classification of compressed breast shapes for the design of equalization filters in x-ray mammography. Medical Physics 1998; 25: 937-948.

3) Zhou C, Chan HP, Petrick N, Helvie MA, Goodsitt MM, Sahiner B, Hadjiiski LM. Computerized image analysis: Estimation of breast density on mammograms. Medical Physics (submitted)

4) Johns HE and Cunningham JR. *The Physics of Radiology*, Fourth Edition, Charles C. Thomas, Springfield, IL 1983.

5) Saloman E and Hubbell J. X-ray attenuation coefficients (total cross sections): Comparison of the experimental data base with recommended values of Henke and the theoretical values of Scofield for energies between 0.1-100 keV, National Bureau of Standards Rep. NBSIR 86-3431, 1986.

(10) Appendix

The following publications in the current year as a result of this grant are enclosed with this report.

1. Zhou C, Chan HP, Petrick N, Helvie MA, Goodsitt MM, Sahiner B, Hadjiiski LM. Computerized image analysis: Estimation of breast density on mammograms. Medical Physics (submitted)

2. Goodsitt MM, Chan HP, Huang H, Zhou C. Automated spot mammography for improved imaging of dense breasts. Accepted for presentation at the 86th Scientific Assembly and Annual Meeting of the Radiological Society of North America in Chicago, IL, November 26-December 1, 2000 (Abstract to be published in Radiology)

Computerized image analysis: Estimation of breast density on mammograms

Chuan Zhou

Heang-Ping Chan

Nicholas Petrick

Mark A. Helvie

Mitchell M. Goodsitt

Berkman Sahiner

Lubomir M. Hadjiiski

Department of Radiology

The University of Michigan, Ann Arbor

Correspondence:

Heang-Ping Chan, Ph.D.
University of Michigan
Department of Radiology
1500. Medical Center Drive
UHB1F510B
Ann Arbor, Michigan 48109-0030
Email: chanhp@umich.edu

ABSTRACT

An automated image analysis tool is being developed for estimation of mammographic breast density. This tool may be useful for risk estimation or for monitoring breast density change in prevention or intervention programs. In this preliminary study, a data set of 4-view mammograms from 65 patients was used to evaluate our approach. The mammograms were digitized using a laser scanner and the resolution was reduced to a pixel size of 0.8 mm x 0.8 mm. Breast density analysis was performed in three stages. First, the breast region was segmented from the surrounding background by an automated breast boundary-tracking algorithm. Second, an adaptive dynamic range compression technique was applied to the breast image to reduce the range of the gray level distribution in the low frequency background and to enhance the differences in the characteristic features of the gray level histogram for breasts of different densities. Third, rule-based classification was used to classify the breast images into four classes according to the characteristic features of their gray level histogram. For each image, a gray level threshold was automatically determined to segment the dense tissue from the breast region. The area of segmented dense tissue as a percentage of the breast area was then estimated. An observer performance study was performed in which five radiologists provided visual estimates of the percent dense area as well as manually segmenting the dense area by interactive thresholding for each mammogram. A "true" percent dense area for each mammogram was obtained by averaging the manually segmented area over the five radiologists. We found that the histograms of 6% (8 CC and 8 MLO views) of the breast regions did not exhibit the typical characteristic features of the four classes and were misclassified by the computer, resulting in poor segmentation of the dense region. For the images with correct classification, the correlation between the computer-estimated percent dense area and the "truth" was 0.94 and 0.91, respectively for CC and MLO views, with mean bias of less than 2%. The correlation of the radiologists' visual estimates with the "truth" ranged from 0.90 to 0.95 with mean biases ranging from 0.1% to 11%, depending on the radiologists. The results demonstrate the feasibility of estimating mammographic breast density using computer vision techniques and its potential to

improve the accuracy and reproducibility of breast density estimation in comparison with the subjective visual assessment by radiologists.

Keywords: Mammography, computer-aided diagnosis, breast density, breast cancer risk, image segmentation, thresholding.

1. INTRODUCTION

Breast cancer is one of the leading causes for cancer mortality among women[1]. One in every eight women will develop breast cancer at some point in their lives. The most successful method for early detection of breast cancer is screening mammography. Currently, mammograms are analyzed visually by radiologists. Because of the subjective nature of visual analysis, qualitative responses may vary from radiologist to radiologist. Therefore, a computerized method for analyzing mammographic features would be useful as a supplement to the radiologist's assessment. Previous research efforts in computer-aided diagnosis (CAD) for breast cancer detection mainly concentrated on detection and characterization of masses and microcalcifications on mammograms by using computer vision techniques [2]. It has been demonstrated that an effective CAD algorithm can improve the diagnostic accuracy of breast cancer characterization on mammograms, which, in turn, may reduce unnecessary biopsies. In this work, we are studying the feasibility of developing a CAD system for analysis of breast density on mammograms. Studies have shown that there is a strong positive correlation between breast parenchymal density on mammograms and breast cancer risk [3-10]. The relative risk is estimated to be about 4 to 6 times higher for women whose mammograms have parenchymal densities over 60% of the breast area, as compared to women with less than 5% of parenchymal densities.

An important difference between breast density as a risk factor and most other risk factors is the fact that breast tissue density can be changed by dietary or hormonal interventions [7, 11, 12]. Although there is no direct evidence that changes in mammographic breast densities will lead to changes in breast cancer risk, the strong correlation between breast density and breast cancer risk has prompted researchers to use mammographic density as an indicator for monitoring the effects of intervention as well as for studying breast cancer etiology [7, 12-14].

Different methods have been used for evaluation of mammographic breast density. Earlier studies used subjective visual assessment of the breast parenchyma primarily based on the four patterns described by Wolfe [3] (N1 is comprised entirely of fat, P1 has up to 25% nodular densities, P2 has over 25% nodular mammographic densities, DY contains extensive regions of homogeneous mammographic densities). The subjectivity in classifying the mammographic patterns introduced large variability in the risk estimation. Later studies used more quantitative estimates, such as planimetry, to measure the dense area in the breast manually outlined by radiologists on mammograms [4, 8]. These studies indicate that the percentage (%) of mammographic densities relative to the breast area can predict breast cancer risk more accurately than a qualitative assessment of mammographic patterns. Warner et al [15] conducted a meta-analysis of the studies published between 1976 and 1990 to investigate the effect of different methods of classification on estimates of cancer risk. They found that the mammographic parenchymal pattern does correlate with breast cancer risk. The magnitude of the risk varies according to the method used to evaluate the mammograms. With the quantitative estimates of mammographic density, the difference in risk between the highest and the lowest risk category is substantial and is greater than the risks associated with most other risk factors for breast cancer. More recent studies used fractal texture and the shape of the gray level histogram [15] to quantify the parenchymal pattern or used interactive thresholding on digitized mammograms to segment the dense area [12, 16]. It was reported that the thresholding method provided a higher risk value than the texture measure or the histogram shape [17]. Other researchers have attempted to calculate a breast density index to model radiologists' perception [18].

In clinical practice, radiologists routinely estimate the breast density on mammograms by using the BI-RADS lexicon as recommended by the American College of Radiology [19] in order to provide a reference for mammographic sensitivity. Because of the lack of a quantitative method for breast density

estimation, researchers often use the BI-RADS rating for monitoring responses to preventive or interventional treatment and the associated changes in breast cancer risk [20]. We have found that there is a large interobserver variability in the BI-RADS ratings among experienced mammographers[21, 22]. An automated and quantitative estimation, as investigated in this study, will provide not only an efficient means to measure mammographic density, but also a reproducible estimate that will reduce the inter- and intraobserver variability of mammographic density measurements. This image analysis tool will therefore allow researchers to study more definitively the relationship of mammographic density to breast cancer risk, detection, prognosis, and mammographic sensitivity, and to better monitor the response of a patient to preventive or interventional treatment of breast cancers.

2. MATERIALS AND METHODS

2.1. Database

A data set consisting of 260 mammograms of 65 patients was used for development of the histogram analysis method in this study. Each case contains the craniocaudal (CC) view and the mediolateral oblique (MLO) view of both breasts of the patient. The mammograms were selected from the files of patients in the Radiology Department at the University of Michigan. The mammograms were acquired with mammography systems approved by the Mammography Quality Standards Act (MQSA) and were digitized with a LUMISYS 85 laser film scanner with a pixel size of 50 μm X 50 μm and 4096 gray levels. The gray levels are linearly proportional to optical densities (O.D.) from 0.1 to greater than 3 O.D. units. The nominal O.D. range of the scanner is 0-4 with large pixel values in the digitized mammograms corresponding to low O.D. The full resolution mammograms were first smoothed with a 16 X 16 box filter and subsampled by a factor of 16, resulting in 800 μm X 800 μm images of approximately 225 X 300 pixels in size.

2.2. Breast segmentation and image enhancement

The breast image is first segmented from the surrounding image background by boundary detection. The detected boundary separated the breast from other background features such as the directly exposed area, patient identification information, and lead markers. The density analysis was performed only within the breast region. An automated breast boundary tracking technique developed previously [23, 24] was modified to improve its performance. Briefly, the technique used a gradient-based method to search for the breast boundary. The background of the image was estimated initially by searching for the largest background peak from the gray level histogram of the image. After subtracting this background level from the breast region, a simple edge was found by a line-by-line gradient analysis from the top to the bottom of the image. The criterion used in detecting the edge points was the steepness of the gradient of four adjacent pixels along the horizontal direction. The steeper the gradient, the greater the likelihood that an edge existed at that corresponding image point. The simple edge served as a starting point for a more accurate tracking algorithm that followed. The tracking of the breast boundary started from approximately the middle of the breast image and moved upward and downward along the boundary. The direction to search for a new edge point was guided by the previous edge points. The edge location was again determined by searching for the maximum gradient along the gray level profile normal to the tracking direction. Since the boundary tracking was guided by the simple edge and the previously detected edge points, it could steer around the breast boundary and was less prone to diversion by noise and artifacts. The unexposed film area around the film edges was detected automatically. After the breast boundary was found, a region growing algorithm was used to fill the enclosed breast region. The result was a binary map that distinguished the breast region from the

background areas. An example of the tracked breast boundary and the breast binary map is shown in Fig. 1(a)-(c).

For the MLO view mammograms, an additional step has to be performed for segmentation of the pectoral muscle. The initial edge in the pectoral region was found as the maximum gradient point by a line-by-line gradient analysis from the chest wall to the breast boundary. The false pectoral muscle edge points were discarded by an edge validation process. First, a straight line was fitted to the initial edge points, and the points that did not lie close to the fitted line were removed. Second, the remaining edge points that were connected were identified by an 8-connectivity criterion. An edge segment was removed if its direction was inconsistent with the pectoral edge direction relative to the breast image. Finally, a second order curve was fitted to the remaining edge points to separate the pectoral muscle from the breast region. The pixels in the pectoral muscle region were excluded from the histogram analysis and breast area calculation. Figure 1 shows the pectoral muscle trimming result for an MLO view mammogram.

To facilitate histogram analysis, a dynamic range compression method was developed to reduce the gray level range of the histograms. With our digitization, the gray levels of the dense tissue are higher than those of the adipose tissue. Because of variations in exposure condition and breast thickness near the periphery, the gray level distribution corresponding to the breast parenchymal pattern is superimposed on a low frequency background that mainly represents the global variations in exposure. This low frequency background distorts the characteristic features of the histogram due to the density pattern. To reduce the distortion, an adaptive dynamic range compression technique was applied to the breast image. For a given breast image, $F(x, y)$, which contains low-frequency background and higher-frequency breast tissue structures, a smoothed image, $F_B(x, y)$, was obtained by applying a large-scale

box filter to $F(x, y)$ to remove the high frequency components while retaining the low frequency components. The image $F_B(x, y)$ was then compressed by a scale factor k:

$$F_C(x, y) = kF_B(x, y) \tag{1}$$

To reconstruct the high frequency components, $F_C(x, y)$, was subtracted from a constant gray level G, and added to the original image, $F(x, y)$:

$$F_D(x, y) = G - F_C(x, y) \tag{2}$$

$$F_E(x, y) = F_D(x, y) + F(x, y) \tag{3}$$

Histogram analysis was applied to the dynamic-range-compressed image $F_E(x, y)$. Figure 2 shows an example of the resulting images and gray level histograms obtained from this procedure, where the size of box filter is 35 X 35, the scale factor k is 0.5, and the constant gray level G is the maximum gray level of the compressed image $F_C(x, y)$.

2.3. Breast density segmentation and estimation

A rule-based threshold technique was developed to segment the dense areas from the breast background. The histogram of the breast region on the dynamic-range-compressed mammogram was generated and smoothed. The histograms of these images in the database were analyzed to formulate an automatic thresholding routine. The histograms were grouped into four classes based on the characteristic shapes of their histograms. It was observed that the grouping corresponded approximately to the four BI-RADS breast density ratings: Class I corresponded to breasts of almost entirely fat, Class II corresponded to scattered fibroglandular densities, Class III corresponded to heterogeneously dense, and Class IV corresponded to extremely dense breasts. Examples of typical histograms for these four

classes are shown in Fig. 3. The histograms seemed to follow two basic patterns. In one pattern, there was only one dominant peak, which represented most of the breast structures in the breast region. In the other pattern, in addition to a large peak in the histogram, there was one or two smaller peaks on the right or left side of the large peak. In a majority of the cases, the smaller peak was distinguishable from the large one when the random fluctuation on the histogram was smoothed.

2.3.1. Peak detection and feature description

The gray level histogram within the breast area was generated and normalized, and passed through an averaging window to smooth out the random fluctuations. The second derivative of every point on the histogram curve was computed. An example of the histogram and its second derivative curve are shown in Fig. 4. The zero crossing locations were detected by scanning for the positive-to-negative and negative-to-positive changes on the latter curve. If the second derivative was negative between two zero crossing points, it indicated that a peak existed between these two points on the histogram. Normally, as shown in Fig. 4, a peak included the peak point P_0 and two valley points P_1 and P_2 located on the two sides of the peak point. The peak point P_0 was determined by searching for the maximum histogram value between the zero crossing points Z_2 and Z_3, and the P_1 and P_2 points were obtained by searching for the point with minimum histogram value between zero crossing points Z_1, Z_2 and Z_3, Z_4, respectively.

The following peak features can be defined by peak point P_0 and valley points P_1 and P_2:

Energy: $$E = \frac{1}{A}\sum_{i=P_1}^{P_2} f(i) * f(i) \qquad (4)$$

Left-side Energy: $$E_L = \frac{1}{A}\sum_{i=P_1}^{P_0} f(i) * f(i) \quad (5)$$

Right-side Energy: $$E_R = \frac{1}{A}\sum_{i=P_0}^{P_2} f(i) * f(i) \quad (6)$$

Likelihood: $$L = E / E' \quad (7)$$

where $f(.)$ is the histogram curve, A is the total energy of the entire histogram and $A = \sum_{i=0}^{N} f(i) * f(i)$, N is the maximum gray level of the histogram. E' is the energy calculated by approximating the histogram in the interval $[P_1,P_2]$ using two straight lines, P_1P_0 and P_0P_2. The energy E of the peak is used to compare the sizes of the peaks on the histogram, higher energy means bigger size of the peak. E_L and E_R split the energy E into two parts from the peak point for calculating the ratio of the energy in these two parts. The likelihood L describes how close is the real peak to the triangle represented by the three points P_0, P_1 and P_2.

2.3.2. Rule based histogram classification

A rule-based histogram classifier was developed to classify the gray level histogram of the breast area into four classes. As shown in Fig. 3, a typical Class I breast is almost entirely fat, it has a single narrow peak on the histogram. Class II has scattered fibroglandular densities, it has two peaks, other than the tail part on the left, on the histogram, with the smaller peak on the right of the bigger one. Class III is heterogeneously dense, it also has two peaks, but the smaller peak is on the left of the bigger one. Class IV is extremely dense, which has a single dominant peak on the histogram, but it is wider compared with the peak in the Class I histogram, and a second small peak sometimes occurs to the left of the main peak.

The classification is performed in two steps. In the first step, the computer determines whether there is only one single peak in the histogram. The biggest peak (main peak) P_M and its location are detected by comparing the energy of the peaks on the histogram. The single peak feature is mainly determined by the energy under the main peak. If the histogram is found to have a single-peak pattern, in general, a narrow peak corresponds to very fatty breast (Class I), and a wider peak corresponds to very dense breast (Class IV). However, in some cases, the histogram of these two classes is very similar, as discussed below (Fig. 9), and it is difficult to distinguish them by their gray level histogram distributions. Two additional image features were analyzed to classify very fatty and very dense breasts. One feature is the gray level standard deviation (*Std*) in the entire breast area, defined as:

$$Std = \left(\frac{1}{N} \sum_{x \in MAP} \sum_{y \in MAP} (f(x,y) - \bar{f}(x,y))^2 \right)^{1/2} \tag{8}$$

where *MAP* is the breast binary map region, N is the pixel numbers within *MAP*. Another feature is the number of single pixels and single pixel-size holes (*NSH*) counted in the breast area of a segmented binary image using the biggest histogram peak point P_M as a threshold. For a very fatty mammogram, the breast mainly consist of a fatty background with some fibrous structures and fibroglandular tissue scattered in the breast area. The *NSH* value is bigger, and *STD* is smaller, compared with a mammogram of a very dense breast.

In the second step, if the histogram is found to have more than one peak, decision rules are used to decide if the second major peak is on the left side or on the right side of P_M by the features E, E_L, E_R, and L, and the relative position of the two peaks. If the second major peak is on the right, then the histogram is classified to be Class II; otherwise, it is classified to be Class III.

2.3.3. Gray level thresholding

Gray level thresholding is essentially a pixel classification problem. Its objective is to classify the pixels of a given image into two classes: one includes pixels with gray values that are below or equal to a certain threshold, the other includes those with gray values above the threshold. Thresholding is a popular tool for image segmentation, a variety of techniques have been proposed over the years. In our study, two threshold selection methods are used: one is the Discriminant Analysis (*DA*) method [25] and the other is the Maximum Entropy Principle (*MEP*) based method [26]. The *DA* method assumes that the image gray levels can be classified into two classes by a threshold. To estimate the threshold, a discriminant criterion based on the within-class variance and between-class variance is introduced. An optimal threshold is selected by the discriminant criterion to maximize the separability of the resultant classes in terms of gray levels. This method is well-suited for the cases where the gray level histogram is bimodal. In an ideal situation, the histogram has a deep and sharp valley between the two peaks representing objects and background, respectively, and the optimum corresponds to the gray level at the bottom of this valley. A more detailed description of the *DA* method can be found in Appendix A.

For the *MEP* method, the optimal threshold value is determined by maximizing the *a posteriori* entropy subject to certain inequality constraints that are derived by means of special measures characterizing the uniformity and the shape of the regions in the image. As is well-known [27], the *MEP* can serve as a criterion to select *a priori* probability distributions when very little is known about the probability distribution. Compared with the *DA* method, *MEP* can provide a better thresholding result if the gray level histogram does not have a bimodal distribution. A more detailed description of the *MEP* method can be found in Appendix B.

The gray level histograms of the mammograms in our study are very complex, the histogram may be unimodal, bimodal, or multi-modal. It is difficult to select an appropriate threshold by one general threshold selection method. Therefore, we combined both the *DA* and the *MEP* methods, to select a threshold according to the characteristic features of the histogram that has been classified into one of the four classes. Suppose $f(g)$ is the gray level histogram of the breast area. Let $T = Method(f(g) \mid g_1 < g < g_2)$ represent the threshold, *T*, that is selected by use of *Method* in the interval $[g_1, g_2]$ of the histogram $f(g)$, where *Method* can be either the *DA* or *MEP* method. The settings of the interval $[g_1, g_2]$ for the four classes are discussed below and shown in Fig. 3.

Class I: The histogram is unimodal so that the threshold is selected as:

$$T = MEP(f(g) \mid g_1 < g < g_2).$$

where, g_1 is the main peak point, g_2 is the valley point on the right side of main peak.

Class II: The histogram is not unimodal and the histogram is classified as Class II, the threshold is selected by averaging two thresholds that are computed in two different intervals of the histogram by the *DA* method:

$$T_1 = DA(f(g) \mid g > g_1),$$

$$T_2 = DA(f(g) \mid g > g_2),$$

$$T = (T_1 + T_2)/2,$$

where g_1 is the valley on the left of the main peak , g_2 is the main peak point.

Class III: The histogram is not unimodal, there are two possibilities in the histogram distribution: there is a valley between the main peak and its left side peak, as shown in Fig. 3, or no valley exists between

the main peak and its left side peak. In two different intervals of the histogram, two thresholds are computed as:

$T_1 = DA(f(g) \mid g_1 < g < g_2)$,

$T_2 = DA(f(g) \mid g'_1 < g < g_2)$,

where, g_1 is the left valley point of the left-side peak (P_{LM}) of the main peak, g'_1 is the peak point of P_{LM}, and g_2 is right valley point of the main peak. If there is an obvious valley, $T = (T_1 + T_2)/2$, otherwise $T = T_1$.

Class IV: Since the histogram is unimodal, the threshold is computed by the *MEP* method, $T = MEP(f(g) \mid g_1 < g < g_2)$, where, g_1 is the left valley point of the main peak, g_2 is the main peak point.

2.4. Observer Study

In order to compare the accuracy of the computer segmentation method with radiologists' manual segmentation, the data set of 65 patient cases with CC and MLO views of the two breasts, described above, were used in an observer study. A graphical interface was developed for displaying the mammograms and recording the observer's evaluation. The CC-view and MLO-view mammograms for a given breast were displayed side-by-side, a radiologist observer examined the mammograms and gave a BI-RADS rating and a visual estimation of the percent breast density with 10% increments. After the subjective evaluation, each view was displayed sequentially, together with the histogram of the dynamic-range-compressed image. The radiologist would interactively choose a threshold by moving a slider along the abscissas of the histogram plot. The segmented binary image, displayed side-by-side with the mammogram, would change instantaneously when the threshold was changed. The radiologist

could inspect if the segmented area corresponded to the dense area on the mammogram. Once the radiologist was satisfied with the segmentation of the dense area, the gray level threshold and the percent dense area derived from this threshold were recorded. The display then moved to the next view of the same breast for evaluation. The mammograms of the other breast for the same patient would then be displayed and evaluated in the same way. The entire process was repeated for each patient until all patients in the data set were evaluated.

Five MQSA-approved radiologists participated in our observer study. To familiarize the radiologists with the experiment and to assist them in their visual estimation of the percent breast density, we had them trained on a separate set of 25 patient cases prior to the evaluation of the actual data set. During the training session, the computer displayed the percent breast dense area to the radiologist, which was obtained by the radiologist's interactive thresholding of the image. The radiologist could then compare the manually segmented percentage with their visually assessed percent density for the image. This feedback helped "calibrate" the radiologists' visual estimates of the percent dense breast area. The percent dense area obtained by interactive thresholding was not displayed during the actual study.

3. RESULTS

An example of a typical mammogram from each of the four classes and its corresponding enhanced image, its histogram, the selected threshold and the segmented image are shown in Fig. 5(a)-(d), respectively.

The average percent breast density obtained from manual segmentation by the five trained radiologists for each mammogram was used as the "true standard" of the percent breast density for that

mammogram. The breast region was segmented by the breast boundary tracking technique, and the pectoral muscle was trimmed for the MLO-view mammograms. The breast boundary was accurately tracked on 92.3% (240/260) of the mammograms, and the pectoral muscle was correctly trimmed on 74.6% (97/130) of the MLO views. The histograms of 6% (8 CC views and 8 MLO views) of the breast regions did not exhibit the typical characteristic features of the four classes and were misclassified by the computer, resulting in poor segmentation of the dense region.

Figure 6 shows a comparison of the percent breast density visually estimated by radiologists against the true standard for the 94% of the 260 mammograms that were classified correctly by the computer. Table I summarizes the comparison of the radiologists' visual estimates with the true standard. The "difference" between the estimated % breast density and the true standard was calculated for each case, and the mean and the standard deviation of this difference over all cases were estimated for each radiologist and shown in the table. Therefore, the mean difference was the average bias of the estimated % breast density from the true standard over all images in the data set. It can be seen that almost all radiologists had a positive bias, on average, when they visually estimated mammographic density, except for Radiologist 5 who had a small negative average bias on the CC view reading. For a given radiologist, the over-estimation increased as the breast density increased. Although the correlation coefficients were high, ranging from 0.90 to 0.95, the deviations from the diagonal line were systematic. The average bias from the true standard varied from less than 1% to 11%, depending on the radiologist. The root-mean-square (RMS) errors of the five radiologists relative to the true standard ranged from 7.5% to 16.3%.

Figure 7 shows the comparison of the percent breast density between the computer segmentation and the true standard for the 94% of mammograms whose histograms were considered to be correctly classified. There was a trend of over-estimation in the very fatty breasts. In the medium dense range,

the variances from the true standard were high. Some images had a large deviation from the diagonal line, indicating that the threshold was incorrectly determined. Table II summarizes the comparison between the computer performance and the true standard. For the CC views with correct histogram classification, the correlation between the computer-estimated percent dense area and the true percent breast density was 0.94, and between the computer and the radiologists' average visual estimate was 0.87 (not plotted). These correlation coefficients were 0.91 and 0.82, respectively, for the MLO-views with correct classification. Although the correlation coefficients of the computer segmentation with the true standard were not better than those of the visual estimates, the average biases of the computer segmentation from the true standard were less than 2%, which were substantially less than those of visual estimates (Table I). This indicates that computerized segmentation is a good alternative to manual segmentation although variances of the automated method will need to be further reduced. The RMS errors of the computer segmentation were also less than those of the radiologists' visual estimates, at 6.1% and 7.2%, respectively, for CC view and MLO view, when the histograms were correctly classified. The biases and RMS errors for the different subsets of images are also shown in Table II. It can be seen that correct histogram classification was the most important factor in reducing the biases and the RMS errors. The contributions by breast boundary detection and pectoral muscle segmentation were minor, on average, for improving the estimation of the percent dense breast area.

Figure 8 shows the comparison of the individual radiologists' manual segmentation against the true standard. For CC views, the RMS difference in the percent breast density between an individual radiologist's manual segmentation and the true standard varied from 2.9% to 5.9% among the five radiologists. For MLO views, the RMS difference varied from 2.8% to 6.2%. The average biases of the five radiologists ranged from -2.8% to 2.2% for the CC views and from -3.1% to 3.0% for the MLO views. The maximum biases of the five radiologists varied from 4.4% to 22.6% for the CC views and from 5.2% to 23% for the MLO views.

The five radiologists provided BI-RADS density ratings for each breast. Although the BI-RADS ratings exhibited large inter-observer variations [21], it is interesting to compare the computer's histogram classification with the BI-RADS ratings. Since there were 260 images, each with 5 radiologists' ratings, there were a total of 1300 rating comparisons. The comparison of the computer and the radiologists' BI-RADS ratings is shown in Table III. It was found that 87.4% of Class I classification have BI-RADS ratings 1 or 2, 92.0% of Class II classifications have density ratings 2 or 3, 83.4% of Class III classifications have density ratings 3 or 4, and 57.1% of Class IV classifications have density rating 4. More detailed analysis of the variability of radiologists' BI-RADS ratings was discussed by Martin et al.[22].

4. DISCUSSION

Radiologists routinely estimate mammographic breast density using the four BI-RADS categories. In studies that require breast density estimation, radiologists' visual estimates of mammographic density were often used as the density measure. Our observer study indicates that interobserver variation between the BI-RADS ratings of five experienced radiologists ranged from –1 to +1. The subjectively estimated percent dense area can deviate from the true standard by as much as 40%, as shown in Fig. 6. These results indicate the need to develop an objective method for estimation of mammographic breast density in order to improve the accuracy and reproducibility of the estimation. A computerized image analysis method for mammographic breast density estimation will be a useful tool for study of breast cancer risk factors and for monitoring the change of breast cancer risk with preventive or interventional treatments.

In this study, we used the average of the percent breast area obtained with interactive thresholding by five experienced radiologists as the true standard. The gray level thresholding method used in this study could achieve a reasonable segmentation of the dense areas on the mammogram because the image was preprocessed with dynamic range compression. The image-based analysis of breast density will not provide the actual percentage of fibroglandular tissue in the breast volume. However, the previous studies that established the correlation between breast density and breast cancer risk were all based on mammographic density. This indicated that mammographic density is a sufficiently sensitive marker for breast cancer risk, although it may be less accurate than volumetric density. Actual measurement of the percentage of fibroglandular tissue volume in the breast, for example, by x-ray penetration with correction for scatter and beam hardening, is difficult because it requires accurate x-ray sensitometry or phantom calibration for each image. These requirements will limit its use to a few laboratories that have specialized equipment and expert physicists. Magnetic resonance breast imaging can also provide volume measurement of dense tissue but it is expensive and not easily accessible. It can be expected that estimation of mammographic breast density by a computerized image analysis method will be a more practical and viable approach, especially when direct digital mammography becomes more widely used in the future.

Our preliminary study indicates that breast density estimation can be performed automatically and accurately (Fig. 7). Although the accuracy of our current algorithm still needs to be improved, it can be seen that the computer segmentation can provide an estimate of the percent breast density with a very small bias (Table II). More importantly, computer segmentation will be more reproducible and consistent than visual estimates. This will improve the sensitivity of studies that depend on evaluation of the change in mammographic density over time or before and after a certain treatment.

Successful segmentation of dense tissue depends strongly on whether a mammogram can be classified correctly into a proper class. A successful classification will likely result in the selection of a near optimal threshold. Conversely, if a mammogram is classified into a wrong class, the threshold will be selected incorrectly. For the mammograms of very fatty breasts, the gray level histogram has the characteristics of Class I which contains one large single peak. These histograms can be distinguished relatively easily from most of the other classes of histograms if those histograms exhibit the typical features. For mammograms of BI-RADS category 2 or 3, there are scattered fibroglandular or heterogeneously densities in the breast. A small peak may be located on the left or on the right, or on both sides of the main peak on the histogram. The histogram could be classified into Class I if the small peak is not large enough and is not detected as a second peak. Otherwise, it would be classified into Class II or Class III, depending on the location of that small peak relative to the main peak of the histogram. For the two-peak pattern histogram, the *DA* threshold selection method is robust if there is an obvious valley between the two peaks. If the valley is flat or not obvious, averaging the two thresholds obtained by the DA method in two different intervals, as designed for this study, can reduce the chance of calculating an incorrect threshold that differs greatly from the optimum, but it also reduces the chance of finding the optimal threshold. Overall, the rules designed for classification of the two-peak patterns seem to perform consistently well for this data set. One of the difficult situations is to distinguish between Class I and Class IV, when the histogram of a very dense breast mimics that of a very fatty breast, as shown in Fig. 9. This image was correctly classified with the additional features, *STD* and *NSH*. However, there were other cases that failed in spite of the additional criteria. The large difference in the optimal threshold locations between these two classes will lead to a large error in the estimated percent breast density if the histogram is misclassified. Further study is needed to more accurately distinguish these two classes.

The dynamic range reduction technique reduces the variability of the gray level histograms and enhances their characteristics. This pre-processing facilitates the classification of the image into the correct class. There are many image smoothing techniques published in the literature. Low pass filtering with a box filter is the simplest choice. The effectiveness of background correction with a box filtered image depends on the box size. We found that a 35 X 35-pixel filter is a good balance between computation time and the capability to remove the high frequency components. The subtraction of the low-pass filtered image from the original image is a form of unsharp masking. The breast boundary is generally enhanced as shown in Figure 2(e). The pixels at the enhanced breast boundary contribute a small peak to the left tail of the gray level histogram of the breast area. Moreover, if dense tissue is present close to the breast boundary, it may not be segmented correctly due to intensity reduction. Other low frequency estimation techniques such as wavelet decomposition will be investigated in future studies.

In this feasibility study, we used a small data set of mammograms to develop a rule-based classifier for the histogram analysis. Although a large fraction of the histograms manifest characteristic features that can be grouped into four classes, corresponding approximately to the four BI-RADS breast density ratings, there are many exceptions. One such example is shown in Fig. 9. This causes misclassification and incorrect thresholding by the histogram classifier. It will be necessary to investigate if other classification strategies can be more effective than a rule-based method. More importantly, the performance of the computer classifier will have to be improved by training with a larger data set and its generalizability evaluated with unknown cases.

5. CONCLUSION

We are developing an image analysis method for automated segmentation of the dense area from mammograms and estimation of the percent mammographic density. Our preliminary study indicates the feasibility of our approach. The computer-estimated mammographic breast density correlate closely with the average manual segmentation by five experienced radiologists and the average bias is much less than that of the radiologists' visual estimation. We have found that correct classification of the histogram shapes is the most crucial step in our approach. The histograms of many mammograms have distinctive characteristics that can be recognized by a rule-based classifier. However, some histograms deviate from these rules and this can lead to misclassification. Further investigation will be needed to design more robust rules or classifiers to improve the classification accuracy. Despite these limitations, we have demonstrated in this preliminary study that estimation of mammographic density can be performed efficiently and accurately by the automated image analysis tool. The fully automated algorithm can provide an objective and reproducible quantitative estimation of mammographic breast density that is expected to be superior to subjective visual assessment and comparable to manual segmentation by radiologists.

ACKNOWLEDGEMENTS

This work is supported by USPHS Grant CA48129, U. S. Army Medical Research and Materiel Command grants (DAMD 17-99-1-9294 and 17-96-1-6514) and by a Career Development Award (B.S) from the USAMRMC (DAMD 17-96-1-6012). The content of this paper does not necessarily reflect the position of the government and no official endorsement of any equipment and product of any companies mentioned in this paper should be inferred.

APPENDIX

A. Gray-level thresholding - Discriminant Analysis (*DA*) Method

Suppose the probability of the gray level n_i in an image with L gray levels can be estimated as:

$$p_i = n_i / N, \qquad N = \sum_{i=1}^{L} n_i \tag{A.1}$$

If the pixels in the image are classified into two classes C_0 and C_1 by the threshold k, then the probabilities of class occurrence and the class mean levels are given by:

$$\omega_0 = \sum_{i=1}^{k} p_i = w(k), \quad \omega_1 = \sum_{i=k+1}^{L} p_i = 1 - w(k) \tag{A.2}$$

$$\mu_0 = \sum_{i=1}^{k} i p_i / \omega_0 = \mu(k) / \omega_0, \quad \mu_1 = \sum_{i=k+1}^{L} i p_i / \omega_1 = \frac{\mu_T - \mu(k)}{1 - \omega(k)} \tag{A.3}$$

where

$$\omega(k) = \sum_{i=1}^{k} p_i \ , \ \mu(k) = \sum_{i=1}^{k} i p_i \ \text{ and } \ \mu_T = \sum_{i=1}^{L} i p_i$$

are the zeroth- and the first-order cumulative moments of the histogram up to the *k*th level, and the total mean level of original image, respectively.

The between-class variance is defined as

$$\begin{aligned} \sigma_B^2(k) &= \omega_0(\mu_0 - \mu_T)^2 + \omega_1(\mu_1 - \mu_T)^2 \\ &= \omega_0\omega_1(\mu_1 - \mu_0)^2 \\ &= \frac{[\mu_T\omega(k) - \mu(k)]^2}{\omega(k)[1 - \omega(k)]} \end{aligned} \tag{A.5}$$

and the optimal threshold k^* is given by:

$$\sigma_B^2(k^*) = \max_{1 \le k \le L} \sigma_B^2(k). \tag{A.6}$$

B. Gray-level thresholding – Maximum Entropy Principle (*MEP*) Method

Suppose the probability of the gray level n_i in an image with L gray levels can be estimated as:

$$p_i = n_i / N, \qquad N = \sum_{i=1}^{L} n_i \tag{B.1}$$

After thresholding the image by threshold k, the *a posteriori* probability of the pixels with gray level value less than k is given by:

$$F(k) = \sum_{i=0}^{k} p_i \tag{B.2}$$

And the *a posteriori* probability of all those pixels with values greater than or equal to k is *1-F(k)*. Thus the Shannon entropy of the thresholded image is:

$$H(F(k)) = -F(k)\log F(k) - (1 - F(k))\log(1 - F(k)) \tag{B.3}$$

The optimal threshold k maximizes *H(F(k))*.

REFERENCES

[1]S. H. Landis, T. Murray, S. Bolden, and P. A. Wingo, "Cancer statistics, 1998," CA Cancer J Clin 48, 6-29 (1998).

[2]H.-P. Chan, N. Petrick, and B. Sahiner, *Computer-aided breast cancer diagnosis. In: Soft Computing Techniques in Breast Cancer Prognosis and Diagnosis*, L. C. Jain, (CRC Press, New York, 2000).

[3]J. N. Wolfe, "Breast patterns as an index of risk for developing breast cancer," Am. J. Roentgenol. 126, 1130-1139 (1976).

[4]J. N. Wolfe, A. F. Saftlas, and M. Salene, "Evaluation of mammographic densities: A case-control study," AJR 148, 1087-1092 (1987).

[5]N. F. Boyd, B. O'Sullivan, E. Fishell, and e. al., "Mammographic patterns and breast cancer risk: methodologic standards and contradictory results," J. Natl. Cancer Inst. 72, 1253-1259 (1984).

[6]A. F. Saftlas and M. Szklo, "Mammographic parenchymal patterns and breast cancer risk," Epidemiologic Reviews 9, 146-174 (1987).

[7]J. Brisson, R. Verreault, A. S. Morrison, D. Tennina, and F. Meyer, "Diet, mammographic features of breast tissue, and breast cancer risk," Am. J. Epidemiology 130, 14-24 (1989).

[8]A. F. Saftlas, R. N. Hoover, L. A. Brinton, M. Szklo, D. R. Olson, M. Salane, and J. N. Wolfe, "Mammographic densities and risk of breast cancer," Cancer 67, 2833-2838 (1991).

[9]A. M. Oza and N. F. Boyd, "Mammographic parenchymal patterns: A marker of breast cancer risk," Epidemiologic Reviews 15, 196-208 (1993).

[10]C. Byne, "Studying mammographic density: Implications for understanding breast cancer," J. Natl. Cancer Inst. 89, 531-532 (1997).

[11]W. Leung, F. Goldberg, B. Zee, and E. Sterns, "Mammographic dnesity in women onpostmenopausal hormone replacement therapy," Surgery 122, 669-674 (1997).

[12]N. F. Boyd, C. Greenberg, G. Lockwood, L. Little, L. Martin, J. Byng, Y. Martin, and D. Tritchler, "Effects at two years of a low-fat, high--carbohydrate diet on radiologic features of the breast: Results from a randomized trial," J. Natl. Cancer Inst. 89, 488-467 (1997).

[13]D. V. Spicer, G. Ursin, Y. R. Parisky, J. G. Pearce, D. Shoupe, A. Pike, and M. C. Pike, "Chenges in mammographic densities induced by a hormonal contraceptive designed to reduce breast cancer risk," J. Natl. Cancer Inst. 86, 431-436 (1994).

[14]C. Byne, C. Schairer, J. N. Wolfe, N. Parekh, M. Salane, L. A. Brinton, R. Hoover, and R. Haile, "Mammographic features and breast cancer risk: Effects with time, age, and menopause status," J. Natl. Cancer Inst. 87, 1622-1629 (1995).

[15]J. W. Byng, N. F. Boyd, E. Fishell, R. A. Jong, and M. J. Yaffe, "Automated analysis of mammographic densities," Phys Med Biol 41, 909-923 (1996).

[16]S. J. Graham, M. J. Bronskill, J. W. Byng, M. J. Yaffe, and N. F. Boyd, "Quantitative correlation of breast tissue parameters using magnetic resonance and x-ray mammography," British J Cancer 73, 162-168 (1996).

[17]M. J. Yaffe, N. F. Boyd, J. W. Byng, R. A. Jong, R. Fishell, G. A. Lockwood, L. E. Little, and D. L. Tritchler, "Breast cancer risk and measured mammographic density," European J. of Cancer Prevention 7, Suppl. 1, S47-S55 (1998).

[18]J. M. Boone, K. K. Lindfors, C. S. Veatty, and J. A. Seibert, "A breast density index for digital mammograms based on radiologists' ranking," J. Digital Imaging 11, 101-115 (1998).

[19]*American College of Radiology. Breast Imaging - Reporting and Data System (BI-RADS)*, Third Edition ed. (American College of Radiology, Reston, VA, 1998).

[20]E. White, P. Velentgas, M. T. Mandelson, C. D. Lehman, J. G. Elmore, P. Porter, Y. Yasui, and S. H. Taplin, "Variation in mammographic breast density by time in menstrual cycle among women aged 40-49 years," J. Natl. Cancer Inst. 90, 906-910 (1998).

[21]C. Zhou, H. P. Chan, N. Petrick, B. Sahiner, H. M. A, M. A. Roubidoux, L. M. Hadjiiski, and M. M. Goodsitt, "Computerized image analysis: Estimation of breast density on mammograms," Proc. SPIE 3979, 1615-1624 (2000).

[22]K. E. Martin, M. A. Helvie, C. Zhou, M. A. Roubidoux, J. E. Baily, C. Paramagul, and H. P. Chan, "Automatic computer-aided quantitative assessment of mamomgraphic density: A validation study," Washington, DC, May 7-12, 2000.

[23]A. R. Morton, H. P. Chan, and M. M. Goodsitt, "Automated model-guided breast segmentation algorithm," Medical Physics 23, 1107-1108 (1996).

[24]M. M. Goodsitt, H. P. Chan, B. Liu, A. R. Morton, S. V. Guru, S. Keshavmurthy, and N. Petrick, "Classification of compressed breast shape for the design of equalization filters in mammography," Med. Phys. 25, 937-948 (1998).

[25]N. Otsu, "A threshold selection method from gray-level histograms," IEEE Trans. System, Man, Cybernetics 9, 62-66 (1979).

[26]A. K. C. Wong, "A gray-level threshold selection method based on Maximum entropy principle," IEEE Trans. System, Man, Cybernetics 19, 866-871 (1989).

[27]J. N. Kapur, "Twenty-five years of maximum-entropy principle," J. Math. Phys. Sci. 17, 103-156 (1983).

Table I. Comparison of radiologists' visual estimate of mammographic breast density with the true standard. The "Difference" was defined as the difference between the estimated % breast density and the true standard for each case, and the mean and the standard deviation of this difference are tabulated.

Image Subsets	No. of Images	Radiologist	Correlation	RMS Error	Mean Difference	Std. Dev. of Difference
CC view:						
All	130	Rad.1	0.942	13.3%	6.9%	11.5%
		Rad.2	0.931	14.5%	9.8%	10.7%
		Rad.3	0.923	13.3%	6.3%	11.8%
		Rad.4	0.934	7.5%	2.9%	7.0%
		Rad.5	0.901	9.6%	-1.4%	9.6%
Histogram correctly classified	122	Rad.1	0.946	13.7%	7.2%	11.3%
		Rad.2	0.936	14.7%	10.3%	10.8%
		Rad.3	0.929	14.2%	6.7%	11.6%
		Rad.4	0.929	7.7%	3.1%	7.1%
		Rad.5	0.900	9.7%	-1.3%	9.4%
MLO view:						
All	130	Rad.1	0.933	14.5%	8.3%	12.0%
		Rad.2	0.914	16.1%	11.2%	11.5%
		Rad.3	0.915	14.4%	7.7%	12.2%
		Rad.4	0.919	8.8%	4.3%	7.7%
		Rad.5	0.910	9.2%	0.1%	9.2%
Histogram correctly classified	122	Rad.1	0.932	15.0%	8.3%	12.0%
		Rad.2	0.914	16.3%	10.9%	11.4%
		Rad.3	0.919	14.7%	7.8%	12.2%
		Rad.4	0.916	9.0%	4.3%	7.7%
		Rad.5	0.909	9.4%	0.3%	9.2%

Table II. Comparison of computer segmentation with the true standard. The "Difference" was defined as the difference between the estimated % breast density and the true standard for each case, and the mean and the standard deviation of this difference are tabulated.

Image Subsets	No. of Images	Correlation	RMS Error	Mean Difference	Std. Dev. of Difference
CC view:					
All	130	0.746	12.3%	1.3%	12.3%
Boundary correctly tracked	120	0.780	11.4%	1.4%	11.4%
Histogram correctly classified	122	0.943	6.1%	0.2%	6.2%
Boundary & Histogram correctly done	113	0.953	5.6%	0.8%	5.6%
MLO view:					
All	130	0.780	11.6%	1.9%	11.5%
Boundary correctly tracked	120	0.766	11.9%	2.1%	11.7%
Histogram correctly classified	122	0.914	7.2%	1.5%	7.1%
Pectoral muscle correctly trimmed	97	0.733	11.6%	1.6%	11.6%
Boundary & Histogram correctly done	112	0.912	7.2%	1.7%	7.1%
Boundary, Histogram & Pectoral muscle correctly done	83	0.891	7.1%	1.9%	6.8%

Table III. Comparison of computer classification and radiologists' BI-RADS breast density ratings.

Computer classification	BI-RADS 1	BI-RADS 2	BI-RADS 3	BI-RADS 4	Total
Class I	210	262	52	16	540
Class II	0	92	184	24	300
Class III	1	52	167	100	320
Class IV	5	12	43	80	140
Total	216	418	446	220	1300

FIGURE CAPTION

Figure 1. (a) A mammogram from our image database; (b) the image superimposed with the detected breast boundary and pectoral muscle boundary; (c) the binary map of the segmented breast region.

Figure 2. (a) A typical mammogram from our image database; (b) the low frequency image $F_B(x, y)$ obtained by an 35 X 35 box filter; (c) the compressed image $F_C(x, y)$; (d) the inverted image $F_D(x, y)$; (e) the enhanced image $F_E(x, y)$; (f) Gray level histogram within the breast region of the original image $F(x, y)$; and (g) Gray level histogram of the breast region of the enhanced image $F_E(x, y)$.

Figure 3. Four typical classes of histograms and the setting of gray level interval [g_1, g_2] for threshold calculation.

Figure 4. Gray level histogram (solid curve) and the second derivative (dot) curve. P_0 is the peak point, P_1 and P_2 are the valley points of the peak on the two sides of the peak point P_0. Points Z_1, Z_2, Z_3 and Z_4 are zero crossing points on the second derivative curve, which are used for searching the points P_0, P_1 and P_2.

Figure 5. Four classes of typical mammograms and corresponding enhanced and segmented image, histogram and threshold.

Figure 6. Comparison of percent breast density between five radiologists' visual estimates and the true standard. The dash line represents the linear regression of all data points on the plot. (a) CC view, (b) MLO view.

Figure 7. Comparison of percent breast density between the computer segmentation and the true standard. The dash line represents the linear regression of the data on the plot. (a) CC view, (b) MLO view.

Figure 8. Comparison of percent breast density obtained from the five radiologists' manual – segmentation with their average for the same mammograms. (a) CC view, (b) MLO view.

Figure 9. The gray level histograms of two mammograms classified by radiologists as BI-RADS rating 1 (upper mammogram) and BI-RADS rating 4 (lower mammogram). The shapes of the histograms are very similar and cannot be distinguished by our current histogram analysis method. These two examples were correctly classified with the additional *STD* and *NSH* criteria.

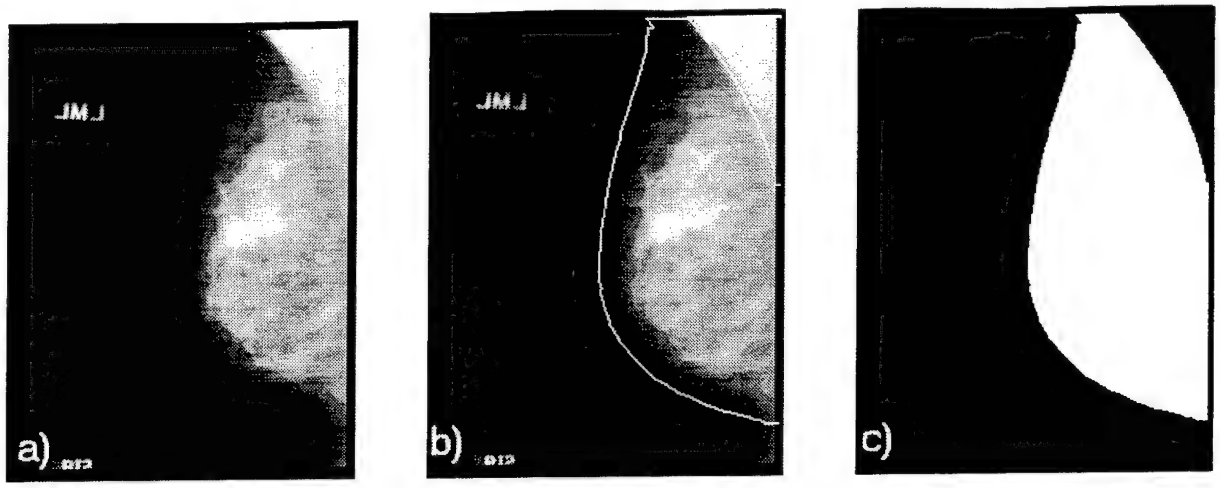

Figure 1. (a) A mammogram from our image database; (b) the image superimposed with the detected breast boundary and pectoral muscle boundary; (c) the binary map of the segmented breast region.

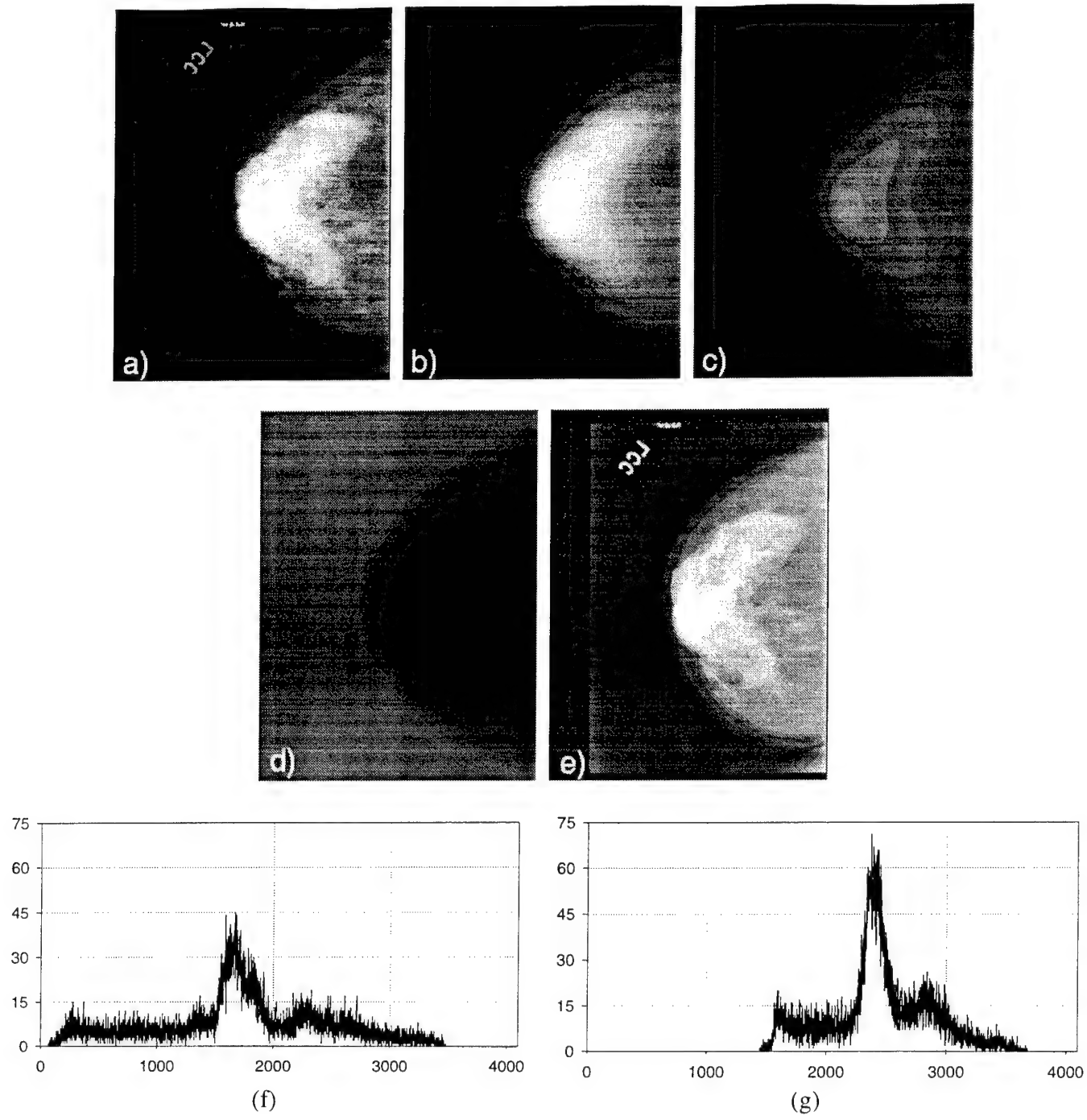

Figure 2. (a) A typical mammogram from our image database; (b) the low frequency image $F_B(x, y)$ obtained by an 35 X 35 box filter; (c) the compressed image $F_C(x, y)$; (d) the inverted image $F_D(x, y)$; (e) the enhanced image $F_E(x, y)$; (f) Gray level histogram within the breast region of the original image $F(x, y)$; and (g) Gray level histogram of the breast region of the enhanced image $F_E(x, y)$.

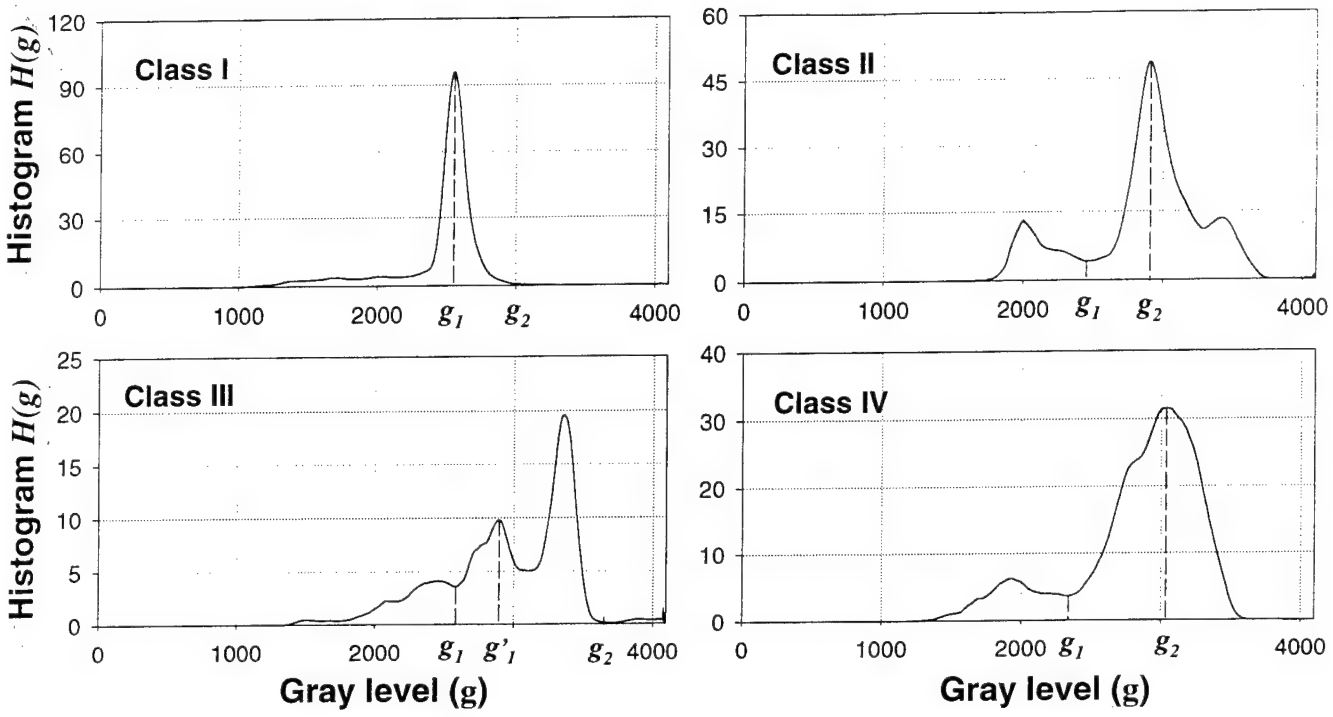

Figure 3. Four typical classes of histograms and the setting of gray level interval [g_1, g_2] for threshold calculation.

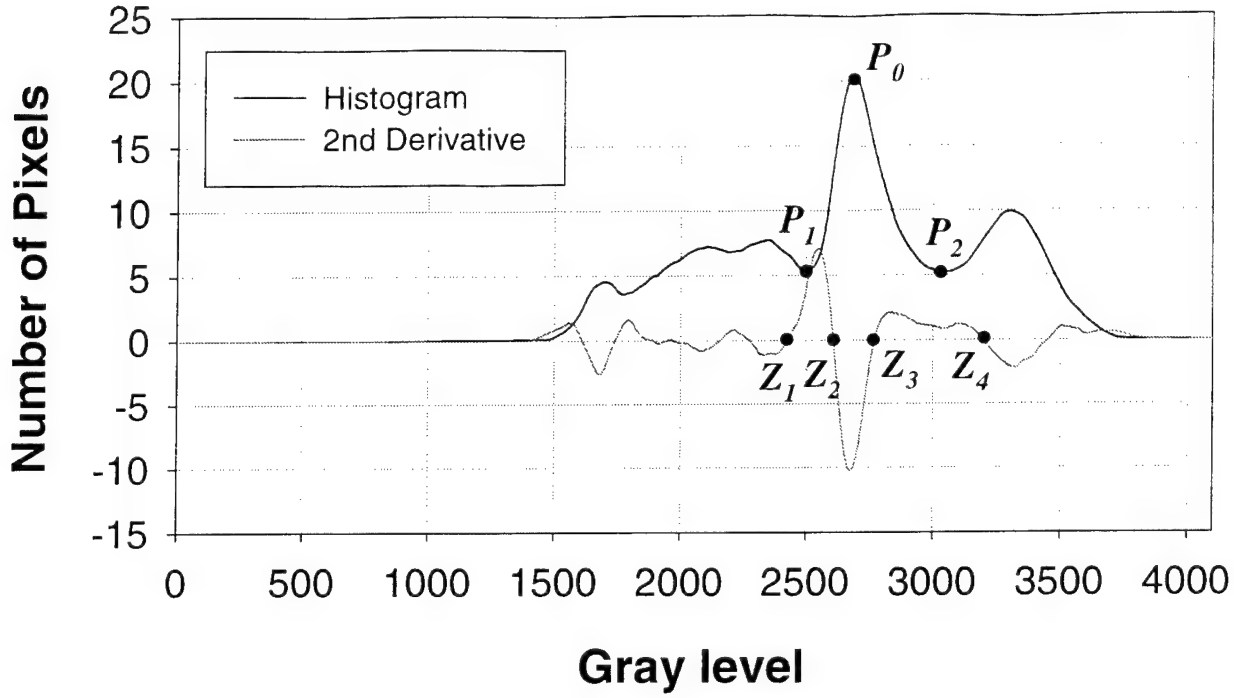

Figure 4. Gray level histogram (solid curve) and the second derivative (dot) curve. P_0 is the peak point, P_1 and P_2 are the valley points of the peak on the two sides of the peak point P_0. Points Z_1, Z_2, Z_3 and Z_4 are zero crossing points on the second derivative curve, which are used for searching the points P_0, P_1 and P_2.

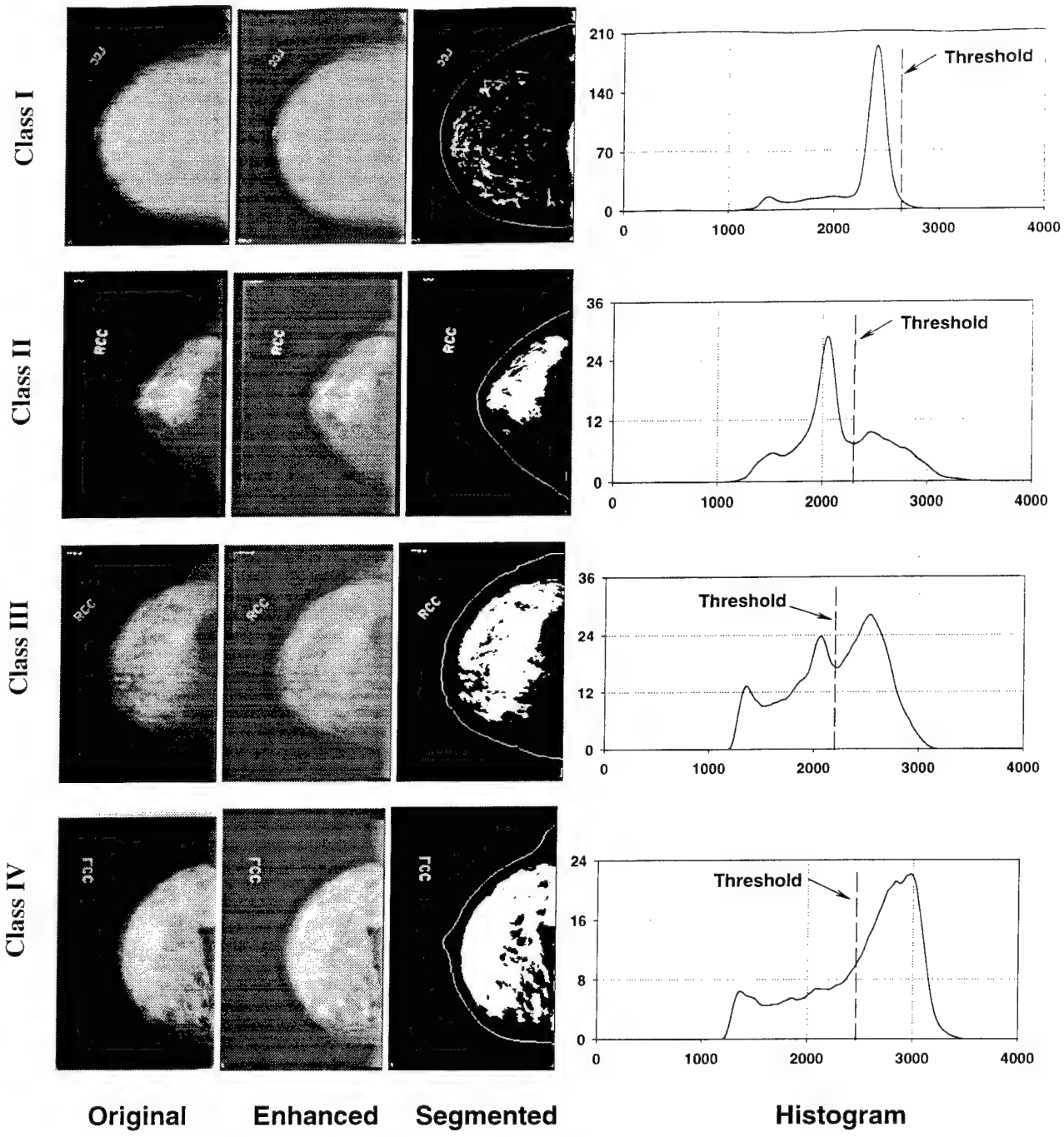

Figure 5. Four classes of typical mammograms and corresponding enhanced and segmented image, histogram and threshold.

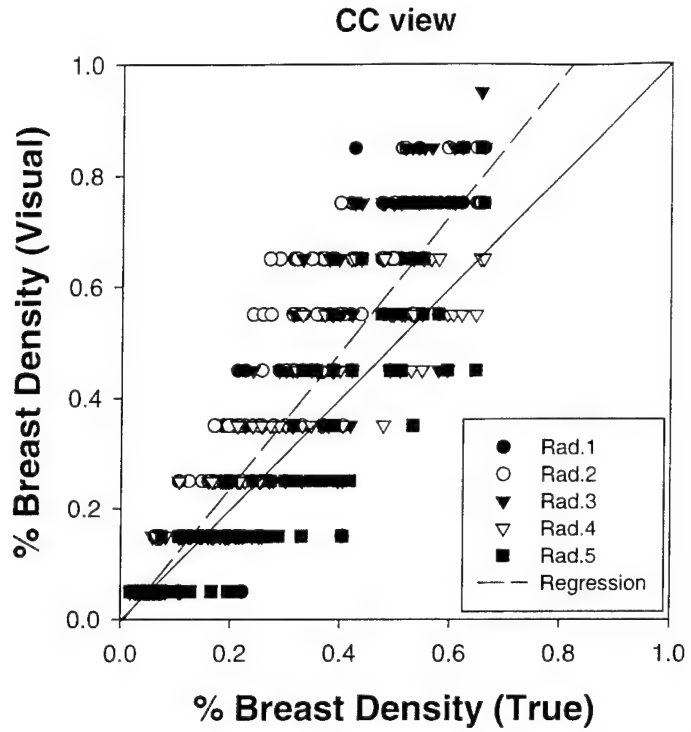

(a)

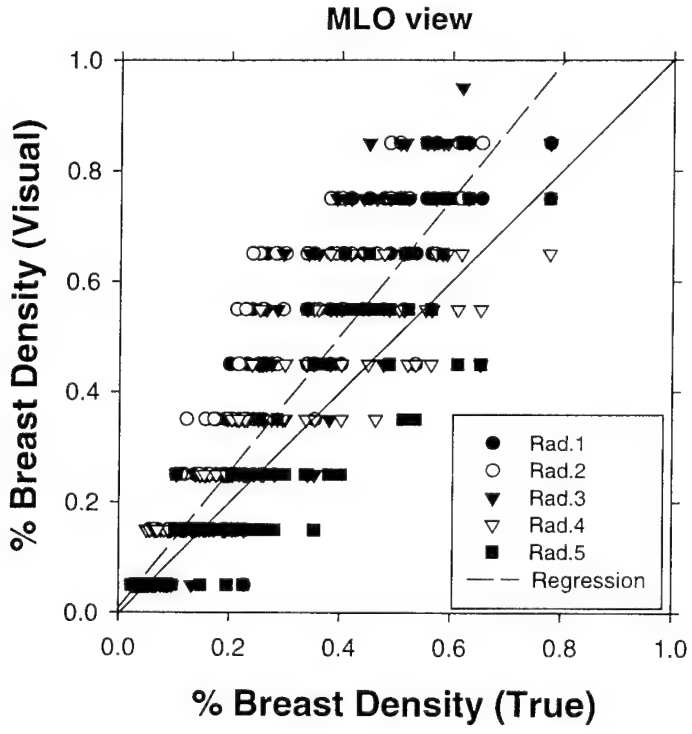

(b)

Figure 6. Comparison of percent breast density between five radiologists' visual estimates and the true standard. The dash line represents the linear regression of all data points on the plot. (a) CC view, (b) MLO view.

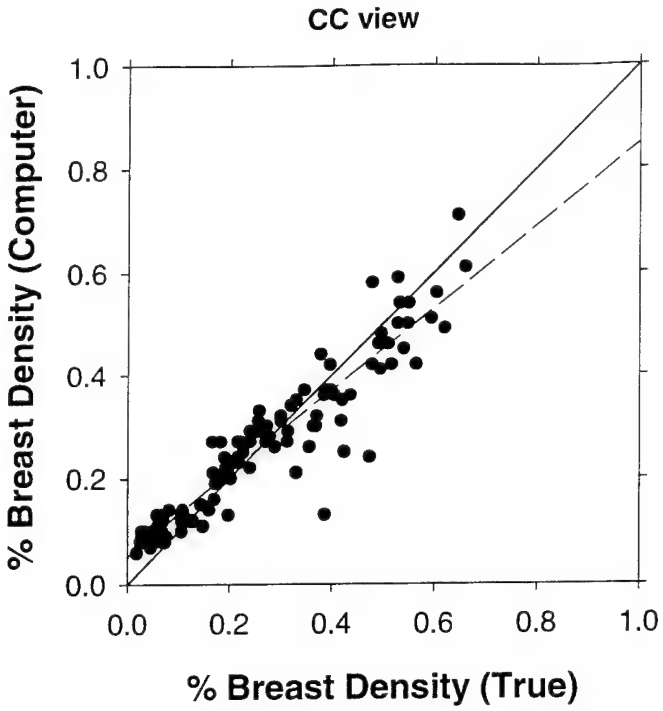

(a)

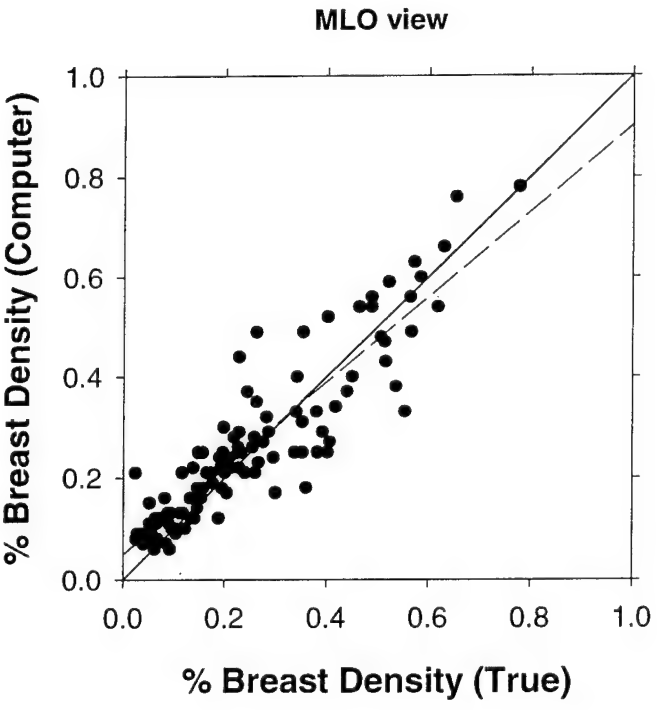

(b)

Figure 7. Comparison of percent breast density between the computer segmentation and the true standard. The dash line represents the linear regression of the data on the plot. (a) CC view, (b) MLO view.

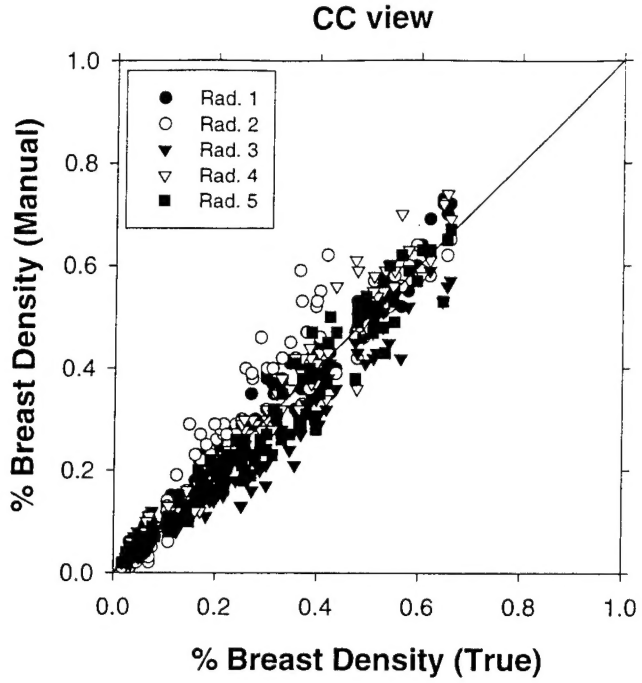

(a)

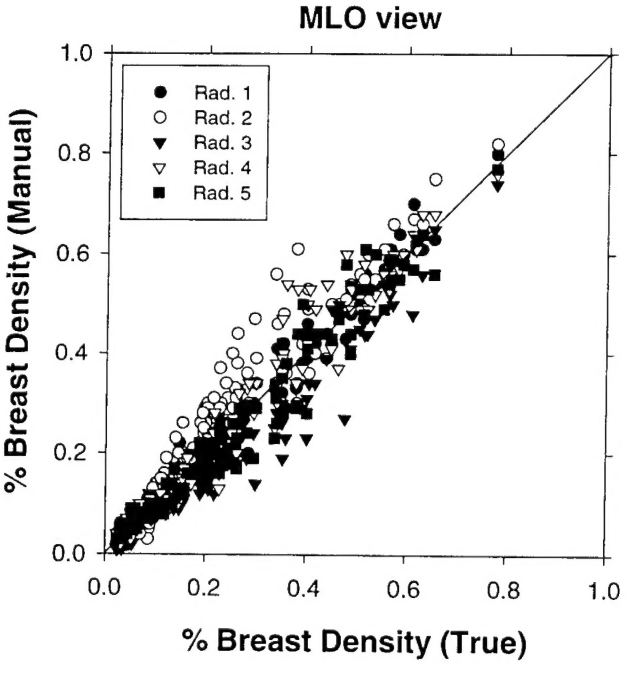

(b)

Figure 8. Comparison of percent breast density obtained from the five radiologists' manual – segmentation with their average for the same mammograms. (a) CC view, (b) MLO view.

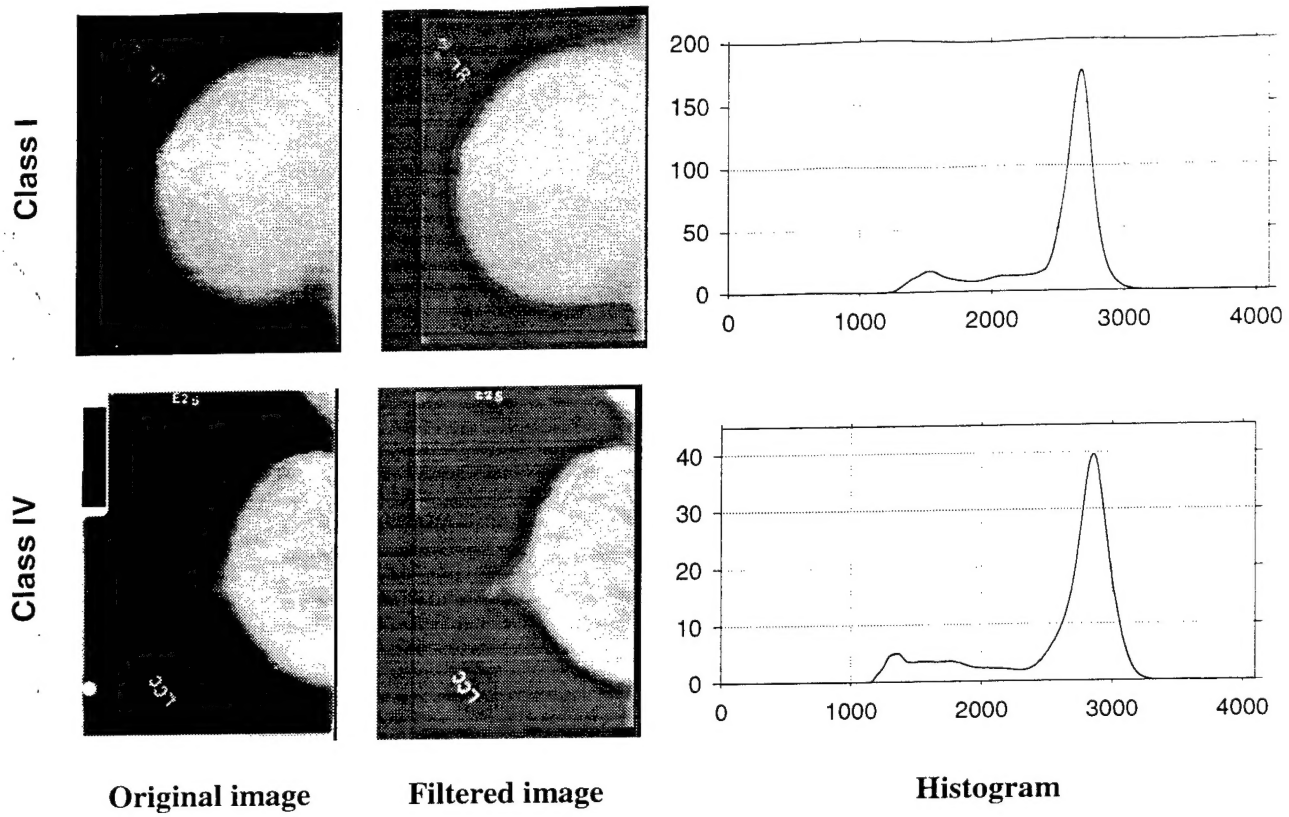

Figure 9. The gray level histograms of two mammograms classified by radiologists as BI-RADS rating 1 (upper mammogram) and BI-RADS rating 4 (lower mammogram). The shapes of the histograms are very similar and cannot be distinguished by our current histogram analysis method. These two examples were correctly classified with the additional *STD* and *NSH* criteria.

ABSTRACT SUBMISSION FOR RSNA 2000
86th Scientific Assembly and Annual Meeting

The corresponding author (to receive confirmation of receipt and acceptance/rejection notice) is:

Mitchell M. Goodsitt Ph.D.

Radiology
University of Michigan
Room B1 F510C, Box 0030
1500 East Medical Center Drive
Ann Arbor, MI 48109-0030 USA
Tel: 734-936-7474
Fax: 734-936-7948
goodsitt@umich..edu

Presentation Type: Scientific Presentation
Category: Physics: Diagnostic X-ray
Keyword 1: Breast radiography, technology
Keyword 2: Physics

Work supported by grant from RSNA: No
Work presented previously: No
Paper submitted for publication: No
Principal Investigator: Other
Presentation Preference: Scientific Paper

Authors

1 Mitchell M. Goodsitt Ph.D. **Phone:** 734-936-7474 **Fax** 734-936-7948
SSN: [redacted] **E-Mail:** goodsitt@umich..edu **Member Number:** **Conflict:** No
2 Heang-Ping Chan Ph.D. **Phone:** 734-936-4357 **Fax** 734-936-7948
SSN: **E-Mail:** chanhp@umich.edu **Member Number:** **Conflict:** No
3 Hao Huang MS **Phone:** 734-647-8556 **Fax**
SSN: **E-Mail:** haohuang@umich.edu **Member Number:** **Conflict:** No
4 Chuan Zhou Ph.D. **Phone:** 734-647-8553 **Fax**
SSN: **E-Mail:** chuan@umich.edu **Member Number:** **Conflict:** No

More than 6 co-authors: No
Presenter #: 1

Title:

Automated Spot Mammography for Improved Imaging of Dense Breasts

Abstract:

PURPOSE:

A primary limitation of conventional screen-film mammography is the inability to adequately image lesions within dense tissue. Because of the low signal-to-noise ratio in dense tissue regions, this will also likely be a problem in digital mammography. We are developing an automated spot mammography technique that should help alleviate this problem. It involves automatically detecting large dense regions within digital mammograms followed by automated x-ray beam collimation and spot compression to generate a second mammogram of only the dense regions.

METHOD/MATERIALS:

Computerized image analysis is applied to a digital mammogram to segment the dense area and identify large dense regions. The minimum sized rectangle or ellipse that bounds the dense region is automatically determined. The coordinates of the bounding region are then employed to position collimator blades via stepper motors in a custom-built asymmetric and rotatable collimator. To attain spot compression at the desired location, the breast is maintained in its original compression position by a special membrane device that is in contact with the breast in front of the conventional compression paddle. The conventional paddle is then removed and replaced by an apparatus that translates the spot paddle to the desired x, y location, and the spot paddle is then moved in to compress the breast.

RESULTS:

Prototype collimator, spot paddle translator, and breast restraining devices have been built. A compressible breast-mimicking phantom containing simulated masses and microcalcifications within dense regions has been designed and is being constructed. Automated spot compression images of the breast phantom obtained with a computed radiography detector will be presented and compared with corresponding images obtained without spot compression and with only spot collimation.

CONCLUSIONS:

Automated spot compression digital mammography is a technique that could be employed in screening to improve imaging of dense tissue regions. Initial experiences with a prototype apparatus will be evaluated with a breast phantom and will be used to develop improved methods for achieving automated spot compression.